Review

Advanced First-Principle Modeling of Relativistic Ruddlesden—Popper Strontium Iridates

Peitao Liu [1] and Cesare Franchini [1,2,*]

1   Faculty of Physics and Center for Computational Materials Science, University of Vienna, Sensengasse 8, A-1090 Vienna, Austria; peitao.liu@univie.ac.at
2   Dipartimento di Fisica e Astronomia, Università di Bologna, 40127 Bologna, Italy
*   Correspondence:cesare.franchini@univie.ac.at

Abstract: In this review, we provide a survey of the application of advanced first-principle methods on the theoretical modeling and understanding of novel electronic, optical, and magnetic properties of the spin-orbit coupled Ruddlesden–Popper series of iridates $Sr_{n+1}Ir_nO_{3n+1}$ (n = 1, 2, and ∞). After a brief description of the basic aspects of the adopted methods (noncollinear local spin density approximation plus an on-site Coulomb interaction (LSDA+U), constrained random phase approximation (cRPA), GW, and Bethe–Salpeter equation (BSE)), we present and discuss select results. We show that a detailed phase diagrams of the metal–insulator transition and magnetic phase transition can be constructed by inspecting the evolution of electronic and magnetic properties as a function of Hubbard U, spin–orbit coupling (SOC) strength, and dimensionality n, which provide clear evidence for the crucial role played by SOC and U in establishing a relativistic (Dirac) Mott–Hubbard insulating state in Sr_2IrO_4 and $Sr_3Ir_2O_7$. To characterize the ground-state phases, we quantify the most relevant energy scales fully ab initio—crystal field energy, Hubbard U, and SOC constant of three compounds—and discuss the quasiparticle band structures in detail by comparing GW and LSDA+U data. We examine the different magnetic ground states of structurally similar n = 1 and n = 2 compounds and clarify that the origin of the in-plane canted antiferromagnetic (AFM) state of Sr_2IrO_4 arises from competition between isotropic exchange and Dzyaloshinskii–Moriya (DM) interactions whereas the collinear AFM state of $Sr_3Ir_2O_7$ is due to strong interlayer magnetic coupling. Finally, we report the dimensionality controlled metal–insulator transition across the series by computing their optical transitions and conductivity spectra at the GW+BSE level from the the quasi two-dimensional insulating n = 1 and 2 phases to the three-dimensional metallic n = ∞ phase.

Keywords: iridates; first-principle methods; computational modeling; spin-orbit coupling; correlated materials; metal-insulator transition

1. Introduction

In the last decade, Ir-based transition metal oxides have become a rapidly evolving research area and have stimulated intensive interest due to the emergence of novel phases of matter and exotic quantum phenomena arising from the cooperative interplay among the crystalline electric field, spin–orbit coupling (SOC), Coulomb repulsion (U), and different spin–exchange interactions (for reviews, see References [1–7]). Of particular interest is the Ruddlesden–Popper (RP) series of iridates $Sr_{n+1}Ir_nO_{3n+1}$ (n = 1, 2, and ∞) [1,8–12]. It is found that, as n increases from 1 to ∞, a dimensionality-controlled insulator–metal transition occurs, revealed by experimentally measured optical conductivity [11] and angle-resolved photoemission spectroscopy (ARPES) [12], associated with a progressive quenching of long-range magnetic ordering. In particular, the first member of the series, Sr_2IrO_4, provides a prototypical model system to investigate entanglement of the spin and orbital degrees of freedom due to a strong SOC, which triggers a novel relativistic J_{eff} = 1/2 Mott-like insulating state in an otherwise metallic compound [8–10,13,14], and an unusual in-plane canted antiferromagnetism (AFM) with a weak net ferromagnetic component [14–17]. The

small gap ($\approx$0.3 eV [18]) is opened by modest Hubbard interactions ($U \approx 1.5$–2 eV [19]) and by strong spin–orbit coupling ($\approx$0.5 eV [20]). In addition, Sr_2IrO_4 exhibits striking structural and magnetic similarities to high-T_c cuprate superconductors such as La_2CuO_4: these two compounds share the same quasi-two-dimensional layered perovskite structure and Ir and Cu have nominal d^5 and d^9 configurations, with one effective hole per site [15,21]. This analogy has boosted the search for superconducting states in a new family of compounds, possibly triggered by doping [22–25] or strain engineering [26]. However, weak evidence for the onset of sperconducting phases has been produced so far. The $n = 2$ compound, $Sr_3Ir_2O_7$, exhibits structural and electronic properties similar to its sister $n = 1$ counterpart Sr_2IrO_4 [27,28]; however, unlike Sr_2IrO_4, it shows a *c*-collinear AFM state and a smaller insulating gap (0.13 eV [29]) [30–33]. The end member of the RP series is the single perovskite $SrIrO_3$. It has a three-dimensional crystal structure, and it has been reported to exhibit a nonmagnetic correlated state combined with a topological crystalline semimetal character [7,11,34–36], The topological state is associated with surface states protected by the lattice symmetry [34,35], a large quasiparticle mass enhancement [11], and an unusual positive magnetoresistance [36].

In this work, we review some results on first-principle modeling of this RP family, putting in evidence the capability of advanced electronic structure methods such as non-collinear local spin density approximation plus an on-site Coulomb interaction (LSDA+U), constrained random phase approximation (cRPA), GW, and the Bethe–Salpeter equation (BSE) to properly account for the novel electronic, magnetic, and optical properties of iridates. We note that most of the results discussed in this review are extracted from our past research on iridates and are therefore unavoidably not exhaustive on many articles dealing with iridates from ab intio perspectives.

2. Methodology

2.1. Noncollinear LSDA+U Model

For a detailed derivation of noncollinear LSDA+U model, we refer to Reference [37]. Here, we just recapitulate the most important aspects of the underlying algorithm— the proper model Hamiltonian on which the noncollinear LSDA+U model is based. To this end, we start from a general on-site Hamiltonian describing the interaction $V_{ij,lk}$ between electrons occupying orbitals i, j, k, l:

$$\hat{\mathcal{H}} = \frac{1}{2} \sum_{i,j,k,l} \sum_{\sigma\xi} V_{ij,lk} \hat{c}_{i,\sigma}^{\dagger} \hat{c}_{j,\xi}^{\dagger} \hat{c}_{k,\xi} \hat{c}_{l,\sigma}, \tag{1}$$

where $\hat{c}_{l,\sigma}$ and $\hat{c}_{l,\sigma}^{\dagger}$, respectively, represent annihilation and creation operators for the orbital l and the spin σ. Using an analogy with the theory of isotropic elasticity [38], where the four-index matrix of elastic constants C_{ijkl} has the same symmetry as $V_{ij,lk}$, the Hamiltonian (1) for the *p*-electron cubic harmonic orbital case can be written exactly as [39]

$$\hat{\mathcal{H}} = \frac{1}{2}\left(U - \frac{J}{2}\right) : \hat{N}^2 : -\frac{J}{4} : \hat{\mathbf{M}}^2 : +\frac{J}{2}\sum_{i,j} : (\hat{n}_{ij})^2 : . \tag{2}$$

where $\hat{N} = \sum_{m,\sigma} \hat{c}_{m,\sigma}^{\dagger} \hat{c}_{m,\sigma}$ is the operator of the total number of electrons on a site; $\hat{n}_{kl} = \sum_{\sigma} \hat{c}_{k,\sigma}^{\dagger} \hat{c}_{l,\sigma}$; and

$$\hat{\mathbf{M}} = \sum_{m,\xi,\xi'} \hat{c}_{m,\xi}^{\dagger} \sigma_{\xi\xi'} \hat{c}_{m,\xi'}$$

is the total magnetic moment vector operator associated with a site. :: denotes normal ordering of creation and annihilation operators, and $\sigma_{\xi\xi'}$ are the Pauli matrices. The normally ordered terms in Equation (2) have the following form [37]:

$$
\begin{aligned}
: \hat{N}^2 : &= \hat{N}^2 - \hat{N}, \\
: \hat{\mathbf{M}}^2 : &= \hat{\mathbf{M}}^2 - 3\hat{N}, \\
: \hat{M}_z^2 : &= \hat{M}_z^2 - \hat{N}, \\
: (\hat{n}_{kl})^2 : &= \sum_{\sigma,\xi} \hat{c}_{k,\sigma}^\dagger \hat{c}_{k,\xi}^\dagger \hat{c}_{l,\xi} \hat{c}_{l,\sigma}.
\end{aligned}
\tag{3}
$$

The first two terms in Equation (2) are essentially the Hamiltonian of the collinear Stoner model on which the collinear LSDA+U models [40–42] are based

$$
\hat{\mathcal{H}} = \frac{U}{2}\left(\hat{N}^2 - \hat{N}\right) - \frac{J}{4}\left(\hat{N}^2 - 2\hat{N}\right) - \frac{J}{4}\hat{M}^2,
\tag{4}
$$

where $\hat{N}_\sigma = \sum_l \hat{n}_{l,\sigma}$, $\hat{N} = \hat{N}_\uparrow + \hat{N}_\downarrow$, and $\hat{M} = \hat{N}_\uparrow - \hat{N}_\downarrow$, with the exception that, in Equation (2), the magnetic moment operator is a vector quantity. However, the Hamiltonian (2) includes an extra third term, required by symmetry and absent in Equation (4). This term is related to the orbital moment of electrons on a lattice site [39].

Following the derivation given in References [40,42], the noncollinear LSDA+U model correction from Hamiltonian (2) equals the difference between the exact and mean-field expectation values of these terms, resulting in [37]

$$
\begin{aligned}
E_{\text{LSDA}+U} - E_{\text{LSDA}} = \\
\left[\frac{1}{2}\left(U - \frac{J}{2}\right) - \frac{J}{4} + \frac{J}{2}\right] \sum_{m,\sigma}\left(n_{m,\sigma} - n_{m,\sigma}^2\right),
\end{aligned}
\tag{5}
$$

where each term in square brackets corresponds to a respective term in Hamiltonian (2) and $n_{m\sigma}$ is the electron occupation number of an orbital state m with spin index σ. The last term $(J/2)\sum_{m,\sigma}\left(n_{m,\sigma} - n_{m,\sigma}^2\right)$, missing in the derivations given in References [40,42], results from the last term in Equation (2). It is clear from Equation (5) that the terms containing parameter J cancel each other exactly and that only the term proportional to parameter U remains.

Generalizing Equation (5) to the case that is invariant with respect to the choice of electronic orbitals and spin quantization axis results in [37]

$$
\begin{aligned}
E_{\text{LSDA}+U} - E_{\text{LSDA}} &= \frac{U}{2}\left[\text{Tr}\rho - \text{Tr}\rho^2\right] \\
&= \frac{U}{2}\left[\sum_{m,\sigma}\rho_{mm}^{\sigma\sigma} - \sum_{m,\sigma;m',\sigma'}\rho_{mm'}^{\sigma\sigma'}\rho_{m'm}^{\sigma'\sigma}\right],
\end{aligned}
\tag{6}
$$

where ρ is the full orbital and spin-dependent one-electron density matrix. The invariant orbital- and spin-dependent noncollinear form of LSDA+U potential and double counting correction become [37]:

$$
V_{jl}^{\sigma\sigma'} = \frac{\delta E_{\text{LSDA}+U}}{\delta\rho_{lj}^{\sigma\sigma'}} = \frac{\delta E_{\text{LSDA}}}{\delta\rho_{lj}^{\sigma\sigma'}} + U\left[\frac{1}{2}\delta_{jl}\delta_{\sigma\sigma'} - \rho_{jl}^{\sigma\sigma'}\right],
\tag{7}
$$

and

$$
E_{\text{LSDA}+U}^{dc} = \frac{U}{2}\sum_{\sigma,\sigma',j,l}\rho_{jl}^{\sigma\sigma'}\rho_{lj}^{\sigma'\sigma}.
\tag{8}
$$

This shows that, in addition to correcting the prefactor in the formula, an invariant noncollinear LSDA+U model requires convoluting the density matrix over the full set of its orbital and spin indexes.

It should be noted that, although the noncollinear LSDA+U model derived above is for the p-electron case, its extension to other types of shells containing correlated electrons is straightforward by adopting suitable forms of Hamiltonian [39] and it was shown that the terms containing parameter J also cancel exactly for the d-electron orbitals and other types of shells. Equations (7) and (8) remain sufficiently accurate and applicable [37].

Having obtained a corrected noncollinear LSDA+U model, the question of how to obtain the value of parameter U from first-principles remains. The two most common approaches to quantify U fully ab initio are the linear response method by Cococcioni [43] and cRPA [44–46]. We used cRPA, for which the basic aspects are summarized below.

2.2. Constrained Random Phase Approximation

Initially, the cRPA method [44–46] was designed to calculate the U value in order to merge density functional theory (DFT) with dynamical mean field theory (DMFT) [47–49] for the low energy part of the effective electronic Hamiltonian [50–52]. Since the DFT+U method can be regarded as the static limit of DFT+DMFT in terms of self-energy, the cRPA method has also been used in the DFT+U method as a way to reduce dependence on the parameter U in routine DFT+U calculations.

Within the framework of cRPA [44–46,53], the electronic system was subdivided into two subspaces. One subspace describes the correlated degrees of freedom, which are dominant close to the Fermi level (called target correlated subspace), and the remaining part acts as an effective medium, which screens the interaction between the correlated electrons in the correlated subspace. To avoid double counting, all polarization effects between the correlated electrons χ^c that have already been accounted for by the +U term in DFT+DMFT (or DFT+U) were removed from the total irreducible polarizability χ, leading to the rest polarizability χ^r [45,46,53]

$$\chi^r = \chi - \chi^c. \tag{9}$$

The partially screened Coulomb interaction U was then calculated in the random phase approximation (RPA) but using a "constrained" polarizability, i.e., the rest polarizability χ^r [45,46,53]

$$U^{-1} = V^{-1} - \chi^r, \tag{10}$$

where V is the bare (unscreened) Coulomb interaction. From Equations (9) and (10), it is trivial to show that the fully screened interaction W can be recovered by

$$W^{-1} = V^{-1} - \chi = U^{-1} - \chi^c. \tag{11}$$

Finally, the matrix elements of U were evaluated by [45,46,53]

$$U_{ijkl}(\omega) = \iint d\mathbf{r}d\mathbf{r}' w_i^*(\mathbf{r})w_j^*(\mathbf{r}')U(\mathbf{r},\mathbf{r}',\omega)w_k(\mathbf{r})w_l(\mathbf{r}'), \tag{12}$$

where $w(\mathbf{r})$ is the atomic-like local orbtials such as the maximally localized Wannier functions [54,55]. Clearly, the partially screened interaction is essentially frequency-dependent. Its dynamical effects have been discussed in the DFT+DMFT and GW+DMFT methods [56,57]. For the DFT+U method, normally, the orbital-averaged value of static U is adopted [53]:

$$U = \frac{1}{N^2} \sum_i^N \sum_j^N U_{ijij}(\omega = 0), \tag{13}$$

where N is the number of local orbtials within the correlated subspace.

A final note on cRPA is in place here. If the target correlated states form an isolated manifold around the Fermi level, the removal of χ^c from χ in Equation (9) can be performed straightforwardly either in the plane wave basis [46] or in the Wannier function basis [58,59]. However, when the correlated states are strongly entangled with those non-correlated

(usually s or p) states of the system, the target correlated subspace becomes not trivially defined and evaluation of χ^c must be treated carefully. To address this problem, Miyake and Aryasetiawan [60] proposed a method that disentangles the states around the Fermi level such that a minimal basis set in the Bloch domain within a given energy window is developed. In this method, the calculated effective interactions depend strongly on the choice of the energy window [60]. In order to achieve a good representation of the entangled bands, additional non-correlated s/p-like states were suggested to be included in the Wannier projection and the effective interaction was calculated using a weighted polarizability, where the weights were defined as probabilities for Bloch states being correlated [61–63]. Although the form of the polarizability was claimed to follow the Kubo–Nakano formula for the correlated fluctuation response function [62], it was later pointed out and shown by Kaltak [64] that the weights should be corrected by taking into account the contributions to the polarizability from not only the diagonal elements but also the non-diagonal terms of the correlated projectors. For a more detailed deviation of the correlated polarizability based on the Kubo–Nakano formulism, we refer to Reference [64].

2.3. The GW Method

Thanks to the cRPA method, LSDA+U becomes de facto a parameter-free method in the sense that the U value is not taken as an adjustable parameter but calculated from first-principles. The LSDA+U method has thus been proven to be successful in describing the ground state properties for many correlated materials. However, the LSDA+U method is still limited to a one-electron single-determinant picture and cannot be expected to correct for inherent shortcomings of LSDA [65]. In particular, its descriptions on excited state properties such as band gaps and optical spectra are often not satisfactory.

The *GW* approximation to the exchange correlation is derived systematically from many-body perturbation theory using the Green's function formalism [66,67] and provides a good approximation for the self-energy Σ of a many-body system of electrons by including many-body effects in electron–electron interaction. In this method, the self-energy in real space and imaginary time domain is approximated by $\Sigma = -GW$ [66–68], where G is the single-particle Green's function and W is the fully screened Coulomb interaction calculated by Equation (11) within the RPA. The *GW* method has been widely and successfully applied to the calculations of quasiparticle energies for many types of systems (for reviews, see References [69–71]), and the resulting band gaps are often very close to the experimentally measured values [72–79].

In practical *GW* calculations, the initial G and W are usually constructed using the DFT one-electron energies and orbtials. Among many existing different *GW* variants (e.g., in the order of increasing complexities, single-shot *GW* (G_0W_0) [75], eigenvalue self-consistent *GW* (evGW_0) [78], quasiparticle self-consistent *GW* (QSGW) [77,80], fully self-consistent *GW* (scGW) [81–84], and scGW including vertex corrections [85,86]), the G_0W_0 method is usually the most common choice due to its good compromise between accuracy and efficiency. To speed up the *GW* calculations and to extend their applications on large systems, several efforts and advances in different directions have been made, e.g., by lowering the number of unoccupied states [87], by completely eliminating the unoccupied states [88–90], by reducing the scaling with respect to system size [91–94], and by optimizing existing implementations on current high-performance computing systems [95]. However, one should keep in mind that the reasonably satisfactory accuracy of the G_0W_0 method mostly arises from error cancellation due to the lack of self-consistency and the absence of vertex corrections. To achieve a desired accuracy, the starting one-electron energies and orbtials become particularly important [96,97]. A common practice is to choose a suitable exchange-correlation functional that can best represent the ground state of the system under study. For instance, for systems with localized d or f states, DFT+U obtained one-electron energies and orbitals are usually much closer to the ground state as compared to DFT and, hence, is a better starting point for subsequent G_0W_0 calculations [98,99]. This

is the case for iridates where we have shown that DFT+U with the U calculated from cRPA predicts very similar band structures to that of G_0W_0 [100].

In addition to good prediction of quasiparticle energies, in particular, band gaps, the *GW* method has also seen wide applications in other aspects. For instance, the *GW* method enables an elegant combination with DMFT, i.e., *GW*+DMFT [44,101–103], since *GW* self-energy can be diagrammatically formulated in the same many-body framework as DMFT [48,49]. Therefore, for *GW*+DMFT, one actually knows which Feynman diagrams are counted twice, and *GW*+DMFT thus overcomes the fundamental double counting problems in LDA+DMFT [52]. Moreover, the RPA routines of *GW* implementation, with moderate changes, can be readily applied to the cRPA method as well as the RPA to the correlation energy [104,105], since all these methods share the common RPA framework. Furthermore, accurate description of screening by the *GW* method enables it to be very useful in optical spectra calculations when combined with the Bethe–Salpeter equation [70,106,106–112], which will be briefly introduced in the next section.

2.4. The Bethe–Salpeter Equation

From an ab initio perspective, the established state-of-the-art method for calculating neutral excitation energies and optical spectra is to solve the Bethe–Salpeter equation (BSE) for full reducible two-particle polarizability Π by solving a four-point Dyson-like equation [70,106,106–112]:

$$\Pi^{-1} = \chi^{-1} - K, \tag{14}$$

where χ is the independent irreducible two-particle polarizability and K is the interaction kernel, which in the W approximation ($\delta\Sigma/\delta G \approx -W$) can be expressed as [70,106,106–112]:

$$K = V - W, \tag{15}$$

where V is the unscreened Coulomb interaction and W is the screened exchange interaction. Diagrammatically, if the ladder diagrams caused by W are not considered, then the BSE in Equation (14) reduces to the RPA . By taking into account both the bubble and ladder diagrams, the BSE explicitly accounts for the excitonic effects resulting from electron–hole interactions. For reviews on BSE, we refer to References [70,113,114].

In order to obtain precise peak positions in optical spectra, accurate calculations of quasiparticle energies are important, in particular, the size of the band gap. In addition, the electron–hole interactions have to be properly described. Hence, the natural procedure to calculate the optical spectra consists in the solution of the BSE using the *GW* quasiparticle (QP) energies, adopting the static screening W calculated from the RPA for the electron–hole interactions [70]. This approach is referred to as *GW*+BSE and has been widely used to predict the optical spectra of various systems, e.g., molecules, clusters, semiconductors, and insulators [115–122].

In practice, the BSE is recast into the following generalized eigenvalue problem [70,123]:

$$\begin{pmatrix} \mathbf{A} & \mathbf{B} \\ \mathbf{B}^* & \mathbf{A}^* \end{pmatrix} \begin{pmatrix} \mathbf{X} \\ \mathbf{Y} \end{pmatrix} = \Omega \begin{pmatrix} \mathbf{I} & 0 \\ 0 & -\mathbf{I} \end{pmatrix} \begin{pmatrix} \mathbf{X} \\ \mathbf{Y} \end{pmatrix}, \tag{16}$$

where matrices $\mathbf{A}$ and $\mathbf{B}$ read [123]

$$A_{ai,bj} = (\epsilon_a - \epsilon_i)\delta_{i,j}\delta_{a,b} + \langle ib \mid K \mid aj \rangle, \tag{17}$$

$$B_{ai,bj} = \langle ij \mid K \mid ab \rangle. \tag{18}$$

where indices i, j and a, b represent occupied and unoccupied states, respectively. Ω is the eigenvalues of the BSE, i.e., the excitation energies of the system. X and Y are the

two-particle electron–hole eigenstates in the product basis for the electron–hole pairs: $\psi_i(\mathbf{r})\psi_a^*(\mathbf{r}')$ and $\psi_a(\mathbf{r})\psi_i^*(\mathbf{r}')$

$$\langle(\mathbf{r},\mathbf{r}')|X,Y\rangle = \sum_{i,a}\left[X_{ia}\psi_i(\mathbf{r})\psi_a^*(\mathbf{r}') + Y_{ia}\psi_a(\mathbf{r})\psi_i^*(\mathbf{r}')\right]. \tag{19}$$

Obviously, Equation (16) is a complex non-Hermitian eigenvalue problem that is difficult to solve using standard eigenvalue solvers. A common practice to avoid this difficulty in solid-state physics is to neglect the resonant–antiresonant coupling **B**, thereby reducing the problem to a Hermitian eigenvalue problem. This is known as the Tamm–Dancoff approximation (TDA). Although the full solution in Equation (16) that is beyond the TDA can be recast into a solvable quadratic Hermitian eigenvalue problem by using the time-inversion symmetry [123], it was shown that the TDA shows tiny differences in the optical spectra of solids compared to the full solution of the BSE [123]. In addition, going beyond TDA is technically intractable, when the spin–orbit coupling is considered [123]. Hence, for the iridates under study where the SOC plays important roles, the TDA has to be employed [100]. With the BSE eigenvectors X^Λ and eigenvalues Ω_Λ in the TDA in hand, the frequency-dependent macroscopic dielectric function can be calculated as [100,123]

$$\varepsilon(\omega) = 1 - \lim_{\mathbf{q}\to 0} V(\mathbf{q}) \sum_\Lambda \left(\frac{1}{\omega - \Omega_\Lambda + i\eta} - \frac{1}{\omega + \Omega_\Lambda - i\eta}\right)$$
$$\times \left\{\sum_\mathbf{k} w_\mathbf{k} \sum_{v,c}\langle\psi_{c\mathbf{k}}|e^{i\mathbf{q}\cdot\mathbf{r}}|\psi_{v\mathbf{k}}\rangle X_{cv\mathbf{k}}^\Lambda\right\} \times \left\{c.c.\right\}, \tag{20}$$

with the oscillator strengths S_Λ associated with the optical transitions defined by [100]

$$S_\Lambda = \mathbf{Tr}\left[\left\{\sum_\mathbf{k} w_\mathbf{k} \sum_{v,c}\langle\psi_{c\mathbf{k}}|e^{i\mathbf{q}\cdot\mathbf{r}}|\psi_{v\mathbf{k}}\rangle X_{cv\mathbf{k}}^\Lambda\right\} \times \left\{c.c.\right\}\right]. \tag{21}$$

where V is the bare Coulomb interaction, η is a positive infinitesimal, and $w_\mathbf{k}$ is the k-point weights. $\psi_{v\mathbf{k}}$ and $\psi_{c\mathbf{k}}$ refer to occupied and unoccupied one-electron wave functions, respectively. From $\varepsilon(\omega)$, the real part of the optical conductivity is then derived by

$$\mathrm{Re}[\sigma(\omega)] = \frac{\omega}{4\pi}\mathrm{Im}[\varepsilon(\omega)]. \tag{22}$$

Despite of the success of the *GW*+BSE approach, its high computational cost due to unfavorable scaling has limited its use to small or moderate systems. Time-dependent density functional theory (TDDFT) [70,124–126] provides an alternative approach that has been widely used. In this approach, the interacting polarizability Π is obtained by solving the following two-point Dyson-like equation [70]

$$\Pi^{-1} = \chi^{-1} - (V + f_{\mathrm{xc}}), \tag{23}$$

where f_{xc} is the exchange-correlation kernel, which is defined as the derivative of the time-dependent exchange-correlation potential v_{xc} with respect to the time-dependent density [70]. Comparing Equations (14) and (15), one clearly sees that the difference between TDDFT and BSE lies in the interaction kernels, though the two methods are formulated in different notations (two-point vs. four-point). However, like v_{xc}, the exact f_{xc} is unknown, and hence, how to explore an approximate but appropriate form for f_{xc} becomes a central challenging task in the community of TDDFT. Among the existing approximate exchange-correlation kernels, the nanoquanta kernel [127–130] and bootstrap kernel of Sharma [131] are particularly successful in yielding a satisfactory description of the excitonic effects. Nevertheless, the nanoquanta kernel in TDDFT is computationally as expensive as solving the BSE, since the kernel is essentially derived from the BSE and explicit calculations of the two-electron four-orbital integrals are needed. The bootstrap kernel is not derived from

first-principles and its description of bound excitons is not satisfactory [132]. To overcome the slow performances of the *GW*+BSE while maintaining its accuracy to a large extent, several approaches have been proposed focusing on improving the band gaps by using hybrid-functional calculations and/or improving the screening effects by introducing a material-specific model screening-dependent dielectric function [133–138].

3. Computational Details

All first-principles calculations were performed using the Vienna *Ab initio* Simulation Package (VASP) [139,140]. The Perdew–Burke–Ernzerhof (PBE) [141] approximation was employed for the exchange-correlation functional. The spin–orbit coupling was included. The noncollinear LSDA+*U* model of Dudarev et al. [37] was used to treat the noncollinear magnetism. The cRPA method based on the Kubo–Nakano formulism developed by Kaltak [64] was employed to estimate the *U* values. The single-shot G_0W_0 method using the LSDA+*U* obtained one-electron energies and orbitals as a starting point was used to calculate the QP energies. The optical spectra were computed by solving the BSE in the TDA [123]. For detailed information on the computational settings, we refer to References [14,100,142].

4. Results and Discussions

4.1. Crystal Structures

The RP series of iridates $Sr_{n+1}Ir_nO_{3n+1}$ is a family of materials, with *n* being the number of $SrIrO_3$ perovskite layers sandwiched between SrO layers [143]. Figure 1 displays the crystal structures of the three iridates. Sr_2IrO_4 is a single-layered quasi-two-dimensional (2D) compound for which the symmetry is lowered from $I4/mmm$ to $I4_1/acd$ due to the rotation of IrO_6 octahedra along the *c* axis by about 11.5° [144]. Besides rotation, the IrO_6 octahedra is elongated along the *c* axis, giving rise to a bond length ratio $c/a \approx 1.04$ [144]. $Sr_3Ir_2O_7$ exhibits a similar crystal structure to Sr_2IrO_4, but it consists of stacking bilayers of corner-shared IrO_6 octahedra along the *c* axis [145]. The octahedral rotations for the neighboring IrO_6 octahedra in $Sr_3Ir_2O_7$ are opposite not only within each layer but also between the two layers (see Figure 1b). The perovskite-like $SrIrO_3$ is a high-pressure phase and has an orthorhombic three-dimensional (3D) structure [146,147].
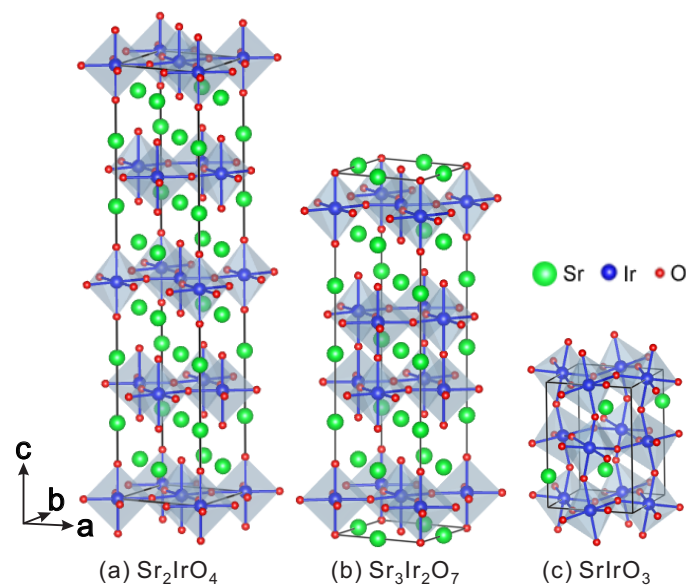

Figure 1. Crystal structure of the Ruddlesden–Popper (RP) series of perovskite-like iridates $Sr_{n+1}Ir_nO_{3n+1}$ (*n* = 1, 2, and ∞). Sr, Ir, and O atoms are shown in green, blue, and red, respectively. Reproduced with permission from Reference [100]. Copyright 2018 by the American Physical Society.

In our calculations, we adopted the experimental lattice parameters and fully relaxed internal atomic positions using the LSDA+U+SOC method until the forces were smaller than 0.01 eV/Å. Experimentally measured magnetic orderings ($n = 1$: in-plane canted AFM [15,17]; $n = 2$: c-collinear AFM [30–33], and $n = \infty$: nonmagnetic [147]) were adopted. The detailed optimized structural and magnetic data are given in Reference [100].

4.2. Electronic Structures

4.2.1. Interplay between U and SOC

For the RP series of iridates, the spin–orbit coupling, electron–electron correlations, and spin–exchange interactions operate with comparable strengths, and depending on their subtle interplay, different phases can develop. Therefore, it is essential to first study how the interplay between U and SOC influences the electronic and magnetic states as well as the transition from one phase to another. Figure 2 shows the metal–insulator transition (MIT) and magnetic phase diagrams of three iridates as a function of Hubbard U and SOC strength. To characterize the strength of SOC, we introduced a factor λ in the SOC term of the Hamiltonian. In this way, one can enhance the effect of the SOC by taking $\lambda > 1$ or can reduce it by taking $\lambda < 1$, where $\lambda = 1$ refers to the self-consistent reference value. The phase diagram displayed in Figure 2 show that the cooperation of U and SOC and dimensionality (n) lead to the formation of different phases: (i) In the limit $U = 0$, all compounds are nonmagnetic metals (NM-M), It can be seen from Figure 2 that, without U ($U = 0$), the three compounds are nonmagnetic metals (NM-M), regardless of the SOC strength. (ii) In the limit of full quenching of SOC strength $\lambda = 0$, a MIT induced by the electron correlation is only achieved for nonphysically large $U > 3$ eV. For smaller U, the systems enter a transient magnetically ordered metal state (AFM-M for $n = 1, 2$ and a more complex magnetic-metal state for $n = \infty$, generally denoted M-M, which will be discussed later on). (iii) The opening of the gap in the Dirac–Mott insulator, $n = 1$ and $n = 2$, is clearly driven by the cooperative action of SOC and U: The general tendency is that, the stronger the SOC strength, the smaller the critical interaction U_c required for opening the gap. For $\lambda = 1$, a moderate $U \approx 1$ eV is sufficient to initiate the MIT in the $n = 1$ and $n = 2$ compounds, whereas a substantially larger value of $U \approx 2$ eV is required for SrIrO$_3$ ($n = \infty$), the only non-insulating member of the considered series. As we will see, the overall predicted ground state, marked by a cross and corresponding to $\lambda = 1$ and U set to the calculated cRPA value, is in excellent agreement with expectations for each member of the series. Our calculated phase diagram for SrIrO$_3$ is consistent with the one reported by Zeb et al. [148].
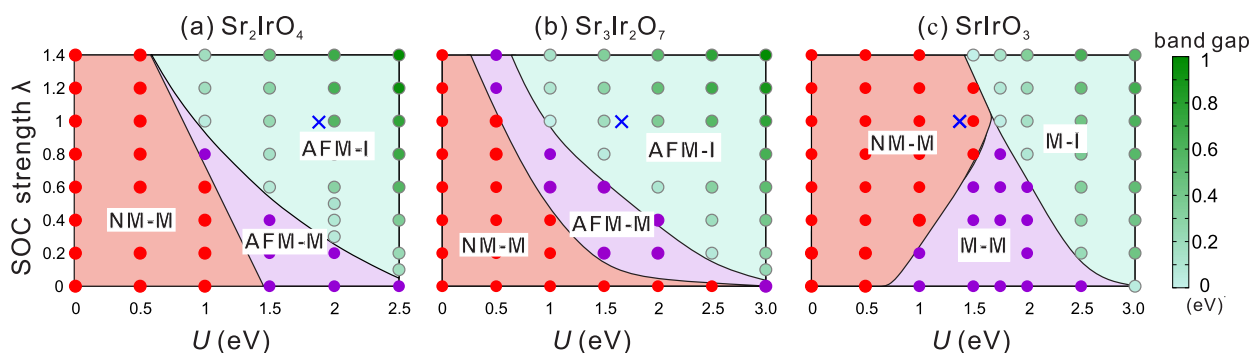

Figure 2. Metal–insulator transition (MIT) and magnetic phase diagrams of three iridates in the $U - \lambda$ space (λ characterises the spin–orbit coupling (SOC) strength, with $\lambda = 1$ being the self-consistent SOC strength). The filled circles are the computed points. The crosses correspond to the constrained random phase approximation (cRPA)-calculated U and therefore mark the first-principle-derived ground state. The right colored bar indicates the value of the band gap (in eV) in the insulating regime. NM-M, AFM-M, AFM-I, M-M, and M-I represent the nonmagnetic metal, antiferromagnetic metal, antiferromagnetic insulator, magnetic metal, and magnetic insulator, respectively.

To further examine the combined effects of U and SOC, we analyzed the band structures shown in Figure 3. In the nonrelativistic ($\lambda = 0$) DFT ($U = 0$) case (Figure 3(a1,b1,c1)), all three iridates are metallic due to partial filling of the t_{2g}^5 bands that crosses the Fermi level. When the SOC is taken into account (Figure 3(a1,b2,c2)), the t_{2g} bands are split into the upper $J_{eff} = 1/2$ and low-lying $J_{eff} = 3/2$ bands (blue curves). Due to the similar crystal structures, Sr_2IrO_4 and $Sr_3Ir_2O_7$ show overall analogous electronic dispersions: the band energies are strongly SOC split at Γ and lifted at the M point. Compared to the nonrelativistic DFT-calculated t_{2g} bands, the bandwidth of the $J_{eff} = 1/2$ manifolds is largely narrowed by the SOC, giving rise to the enhanced Mott instability. In this situation, even a moderate Hubbard U is able to open the band gap, leading to the Mott MIT (Figure 3(a3,b3)). In the 3D perovskite $SrIrO_3$, SOC induces to a k-uniform band-splitting and leads to the emergence of characteristic Dirac-like crossing at the high-symmetry point U [148], which is robust against electronic correlation: a moderate $U = 1$ eV is not sufficient to destroy the Dirac crossing, as shown in Figure 3(c3).
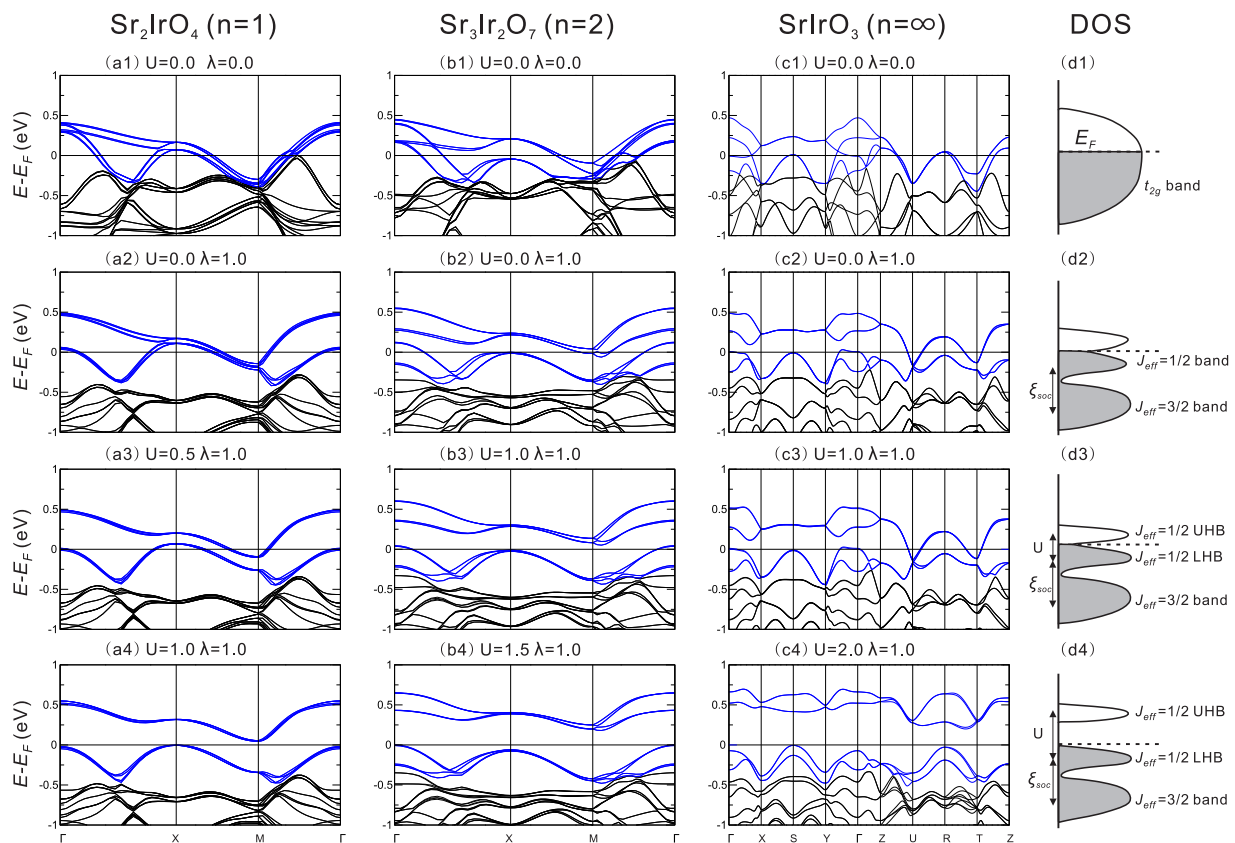

Figure 3. Band structure evolution as a function of Hubbard U and SOC strength λ for three iridates. The Fermi energy has been aligned to zero. The rightmost panel schematically shows the corresponding density of states, with ξ_{soc} being the SOC energy. Note that, to achieve a similar electronic state as in Sr_2IrO_4, a increasingly larger U is used for $Sr_3Ir_2O_7$ and $SrIrO_3$ in the third and fourth rows.

As the Hubbard U is increased further, the band gap formed by the upper and lower Hubbard bands (UHB and LHB, respectively) is increased for $n = 1$ and 2 as well (Figure 3(a4,b4)) and the bands forming the Dirac crossing are split for $n = \infty$ (Figure 3(c4)), causing vanishing of the Dirac state. The larger critical U_c necessary to open the gap increases with dimensionality n and is correlated to the bandwidth, which increases with increasing n. The combined effect of SOC and U is schematized in the model density of states shown in Figure 3(d1–d4), showing the transition from a non-correlated and nonrelativistic metal (Figure 3(d1)) to a full Dirac–Mott state (Figure 3(d4)) through transient states distinguished by the degree of splitting between the lower and upper

$J_{\text{eff}} = 1/2$ bands (Figure 3(d2,d3)). The SOC controls intra-band splitting, causing the formation of $J_{\text{eff}} = 1/2$ and $J_{\text{eff}} = 3/2$ features: U, on the other hand, governs the inter-band splitting between LHB and UHB.

4.2.2. Quantification of Relevant Energy Scales

To quantify the degree of electronic correlations of three iridates and to determine the ground state of each compound in the phase diagram, we calculated the Hubbard U and exchange J by cRPA. The Ir-t_{2g} states are chosen as a target correlated subspace. This choice has been justified by a good match between the nonmagnetic DFT bands and the corresponding ones for the Ir-t_{2g} manifold obtained by Wannier interpolation (see Figure 4). Table 1 summarizes the obtained matrix elements of U_{ij} and J_{ij}. According to Equation (13), we obtained averaged U values of 1.82, 1.67, and 1.37 eV for Sr_2IrO_4, $Sr_3Ir_2O_7$, and $SrIrO_3$, respectively. This is expected, since the gradual increase in bandwidth associated with the increase in dimensionality leads to enhanced screening. With these cRPA values of U, the corresponding DFT+U-predicted ground state for $n = 1, 2$, and ∞, marked with a cross in the phase diagram shown in Figure 2, very well reproduces the experimentally detected electronic ground state: insulating for $n = 1, 2$ and being a metal for $n = \infty$.

Table 1. On-site Coulomb and exchange interactions (in eV) calculated by cRPA for three RP iridates. $U_{ij} = U_{ijij}(\omega = 0)$ and $J_{ij} = U_{ijji}(\omega = 0)$ with i and j representing t_{2g}-like Wannier orbitals. See Equation (12) for the notations used. Reproduced with permission from Reference [100]. Copyright 2018 by the American Physical Society.

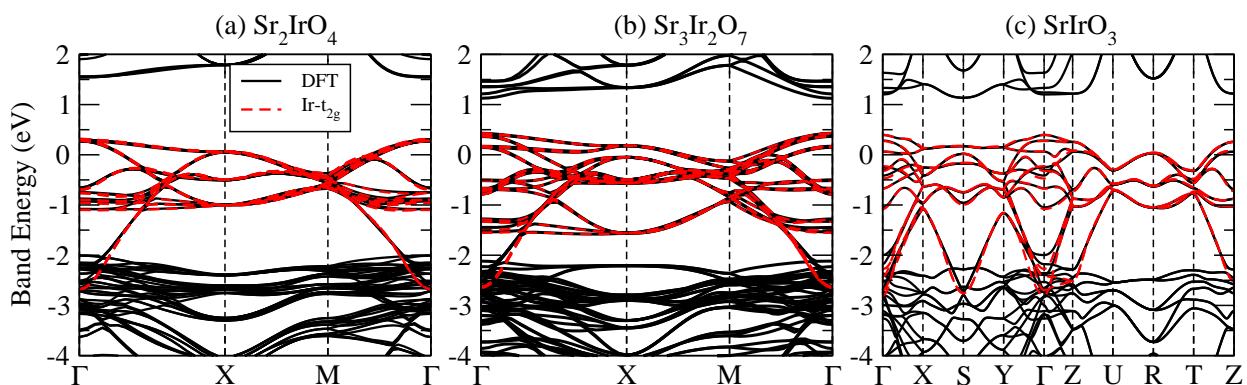|	U_{ij}			J_{ij}		
Sr_2IrO_4	d_{yz}	d_{zx}	d_{xy}	d_{yz}	d_{zx}	d_{xy}
d_{yz}	2.30	1.72	1.57	–	0.23	0.22
d_{zx}	1.72	2.30	1.57	0.23	–	0.22
d_{xy}	1.57	1.57	2.03	0.22	0.22	–
$Sr_3Ir_2O_7$	d_{yz}	d_{zx}	d_{xy}	d_{yz}	d_{zx}	d_{xy}
d_{yz}	2.16	1.58	1.43	–	0.23	0.22
d_{zx}	1.58	2.16	1.43	0.23	–	0.22
d_{xy}	1.43	1.43	1.85	0.22	0.22	–
$SrIrO_3$	d_{yz}	d_{zx}	d_{xy}	d_{yz}	d_{zx}	d_{xy}
d_{yz}	1.78	1.21	1.19	–	0.22	0.22
d_{zx}	1.21	1.73	1.22	0.22	–	0.22
d_{xy}	1.19	1.22	1.74	0.22	0.22	–

Figure 4. The nonmagnetic DFT bands (black line) superposed with Wannier interpolated bands (red dashed line). Reproduced with permission from Reference [100]. Copyright 2018 by the American Physical Society.

To complete the quantification of the other relevant interactions, we also estimated the crystal field energies $10Dq$, the SOC constant λ_{soc}, and the band gap. The data are shown

in Table 2. The $10Dq$ is evaluated from the central mass of density of states between the e_g and t_{2g} bands without U and SOC. The λ_{soc} is approximated as $\lambda_{\mathrm{soc}} \simeq 2/3\xi_{soc}$, with ξ_{soc} being the SOC energy, which is estimated from the total energy difference with and without the inclusion of SOC. One can observe that crystal field energies are the largest energy scale (over 3 eV), and it is thus reasonable to assume the t_{2g} states as the effective total angular momentum $L_{\mathrm{eff}} = -1$. The SOC constant λ_{soc} for three iridates are estimated to be about 0.5 eV, in line with electron-spin resonance measurements (0.40–0.5 eV) [149]. Estimation of the band gap is discussed in the following session, where we assess and compare *GW* and DFT+U.

Table 2. A summary of the space group, Hubbard U, exchange J, crystal field energy $10Dq$, and SOC constant λ_{soc} (eV) as well as DFT+U+SOC- and *GW*+SOC-predicted band gaps. The energy unit is in eV. Experimental gaps are also given for comparison.

	Sr_2IrO_4	**$Sr_3Ir_2O_7$**	**$SrIrO_3$**
Space group	$I4_1/acd$ (142)	$Ccce$ (68)	$Pbnm$ (62)
U	1.82	1.67	1.39
J	0.22	0.22	0.22
$10Dq$	3.70	3.80	4.24
λ_{soc}	0.47	0.49	0.45
Magnetic ordering	*ab*-canted AFM	*c*-collinear AFM	NM
DFT+U+SOC gap	0.23	0.14	metal
GW+SOC gap	0.25	0.16	metal
Expt. gap	0.30 [18]	0.13 [29]	metal [146,147]

4.2.3. *GW* vs. LSDA+U

In this section, we focus on analyzing the ground-state electronic structures in more detail by comparing the LSDA+U+SOC band structure (computed using the cRPA values of U) with the quasiparticle energies obtained by *GW*+SOC.

As shown Figure 5, both approaches reproduce the J_{eff} = 1/2 spin-orbital Mott insulating state of Sr_2IrO_4 and $Sr_3Ir_2O_7$ well and correctly predict $SrIrO_3$ as a semimetal. The obtained fundamental gaps agree well with experimental measurements (see Table 2). However, residual differences are observed between the two methods: *GW* pushes down the O-2p states by about 0.5 eV, which in turn decreases the hybridizations between Ir-d states and O-2p states.

As already mentioned, Sr_2IrO_4 and $Sr_3Ir_2O_7$ exhibit very similar bands. The most noticeable difference is the splitting at the top of the valence band at Γ induced by the bilayer structure in $Sr_3Ir_2O_7$. The computed splitting energy for $Sr_3Ir_2O_7$ is about 0.23 eV, consistent with the one obtained by ARPES [28]. It is important to note that, for both Sr_2IrO_4 and $Sr_3Ir_2O_7$, the J_{eff} = 1/2 LHB and J_{eff} = 3/2 states are not separated by a well-defined gap in contrast to the ideal J_{eff} = 1/2 picture. The band structure of $SrIrO_3$ is semi-metallic and clearly different from the other two compounds. The most important characteristic is the Dirac cone at the U point that is protected by the lattice symmetry [148,150]. The Dirac cone is the only crossing between the conduction and valence band in the entire Brillouin zone and is associated with a pseudogap at the Fermi energy (see Figure 5f,l), in agreement with the experimentally measured small charge carrier density [151], proving the semi-metallic character of $SrIrO_3$.

We note that, although both *GW*+SOC and LSDA+U+SOC capture the main features of three iridates, their descriptions on relative binding energies between the top of the valence band at Γ and X for Sr_2IrO_4 and $Sr_3Ir_2O_7$ are not satisfactory. For instance, ARPES indicates that the maximum of the LHB at Γ lies 150–250 meV lower compared to X for both Sr_2IrO_4 and $Sr_3Ir_2O_7$ [8,25,28,152,153]. However, LSDA+U+SOC predicts that the Γ point is 20 and 70 meV higher in energy than the X points for Sr_2IrO_4 and $Sr_3Ir_2O_7$, respectively. *GW* improves the description only marginally for Sr_2IrO_4, where the top of
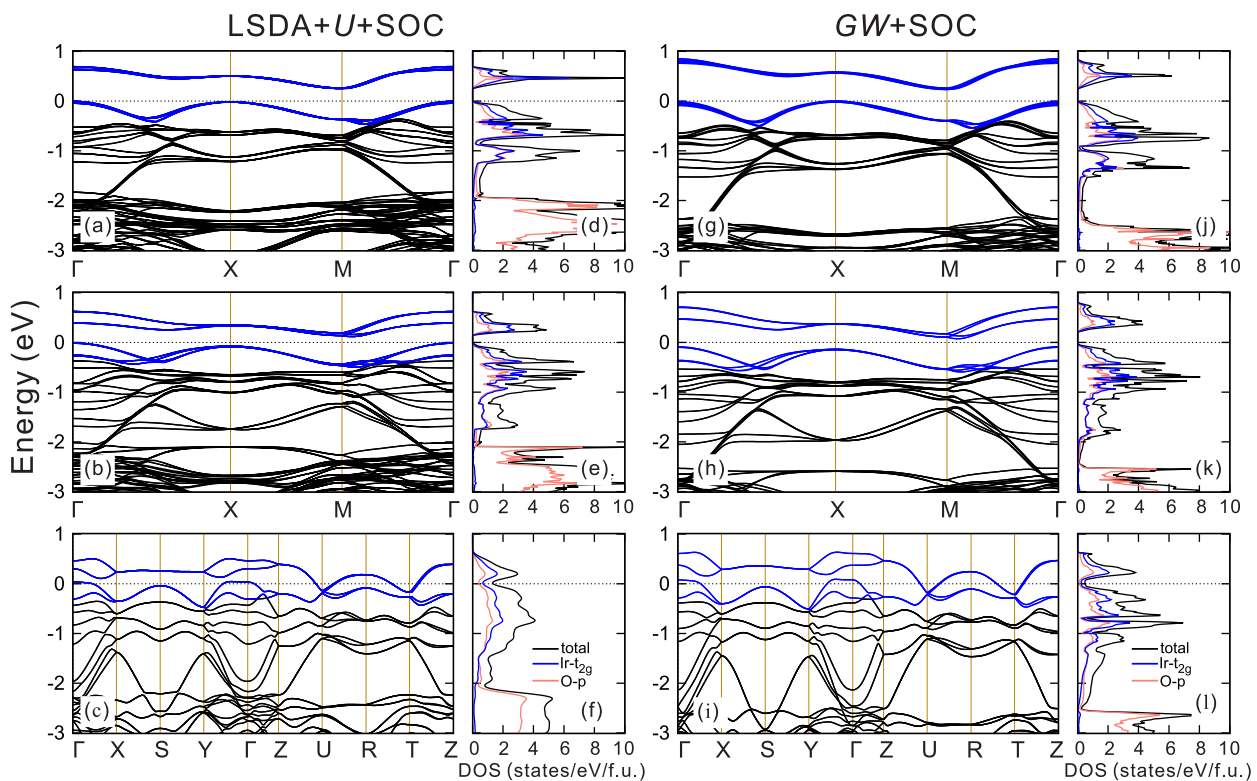
Figure 5. Electronic band structures and density of states (DOS) obtained from (**a**–**f**) LSDA+U+SOC with U calculated from cRPA and (**g**–**l**) GW+SOC calculations for three iridates (upper panel for Sr_2IrO_4, middle panel for $Sr_3Ir_2O_7$, and bottom panel for $SrIrO_3$). The Fermi energy has been aligned to zero. The high-energy Ir-e_g states are not shown due to the large crystal field. Reproduced with permission from Reference [100]. Copyright 2018 by the American Physical Society.

the valence band at X is found 10 meV higher than at Γ but fails in reproducing the correct order for $Sr_3Ir_2O_7$, even though the QP difference $\Gamma - X$ is reduced to 40 meV. A second drawback of the employed level of theory is the reduced degree of electronic correlation for $SrIrO_3$. In fact, GW gives a renormalization factor Z for the $J_{eff} = 1/2$ bands close to the Fermi level of 0.61, yielding a mass enhancement of 1.64, far lower than the experimental value of 6 [11]. This is also reflected by the absence of the characteristic QP peak close to the Fermi level detected by ARPES [152]. These failures imply that the type and degree of correlations included in the GW self-energy are not adequate enough to accurately describe the local band topology of Sr_2IrO_4 and $Sr_3Ir_2O_7$ as well as the correlated metallic state of $SrIrO_3$ and that going beyond the GW approximation is needed, such as DFT+DMFT [154].

Finally, we would like to mention that the gap in Sr_2IrO_4 is unstable upon doping: both electron and hole doping induce an insulator-to-metal transition associated with the emergence of a Fermi surface [153,155,156]. The basic features of the transition are well captured by LSDA+U [142]. Figure 6 show a comparison between calculated (middle panels) and experimental (right panels) Fermi surfaces of $Sr_{2-x}La_xIrO_4$ for different doping concentrations ($x = 0$, 6.25%, and 12.5%). The Fermi surface are extracted from La-doped supercell using the band-unfolding techniques (left panels), whereas the measured data refer to ARPES. The closing of the gap is attributed to a progressive reduction in the electronic correlation in electron-doped samples and by gradual filling of the bottom of the conduction bands. The agreement between theory and experiment is excellent, apart from the feature at Γ in the simulated undoped Fermi surface due to the overestimation of the top of the valence band at Γ, as previously mentioned.
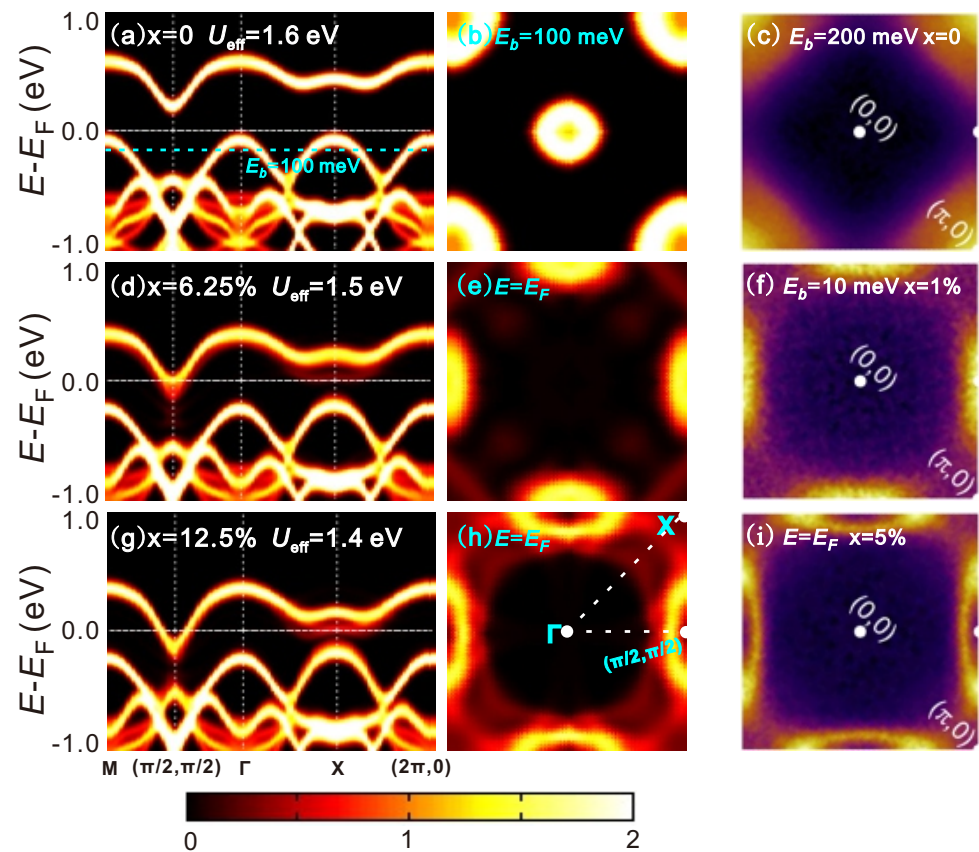
Figure 6. Collapse of the Dirac–Mott gap in electron-doped Sr_2IrO_4 ($Sr_{2-x}La_xIrO_4$). Comparison between calculated bands (left, (**a,d,g**)) and the corresponding Fermi surface [142] (middle, (**b,e,h**)) with the corresponding experimental Fermi surface [153] (right, (**c,f,i**)). Reproduced with permission from Reference [142]. Copyright 2016 by the American Physical Society.

4.3. Magnetic Properties

Now, we turn to a more detailed analysis of the magnetic properties. Figure 7 shows the representative magnetic orderings for the three iridates predicted by LSDA+U+SOC calculations. The computed local magnetic moments including the orbital and spin contributions have been given in Reference [100]. Sr_2IrO_4 exhibits an in-plane canted antiferromagnetic ordering with a weak ferromagnetic moment within the *ab*-plane. The predicted weak ferromagnetic moment is about 0.08 μ_B/Ir, in line with the magnetic susceptibility measurements 0.06–0.14 μ_B/Ir [144,157]. The canting angle of magnetic moment is calculated as 12.5°, in accordance with the x-ray resonant scattering measurement (12.2(8)°) [158].

In contrast to Sr_2IrO_4, $Sr_3Ir_2O_7$ displays an out-of-plane *c*-collinear antiferromagnetic ordering, indicating stronger interlayer couplings. which has been confirmed by the resonant x-ray diffraction [30,32,33]. The nearly zero in-plane magnetic moment is also in agreement with tiny hysteresis in the magnetic susceptibility experiments [30].

Although the magnetic ground state of $SrIrO_3$ is nonmagnetic, its magnetic ordering in the magnetic regime is more complicated due to its distorted three-dimensional crystal structure (see Figure 1c). As illustrated in Figure 7c, the magnetic ordering depends strongly on U and λ. For instance, for $U = 2.0$ and $\lambda = 0.4$, the system shows a canted antiferromagnetic order with a large ferromagnetic component in the *ab* plane (Figure 7(c1)). As λ increases to 1.0, the system becomes a canted A-type antiferromagnet and the moments are largely aligned to the *c* axis (Figure 7(c2)). Keeping $\lambda = 1.0$ and increasing U (compare Figure 7(c2,c3)), the agenetic moments are aligned in a very different way, but the average magnetization per unit cell is zero.
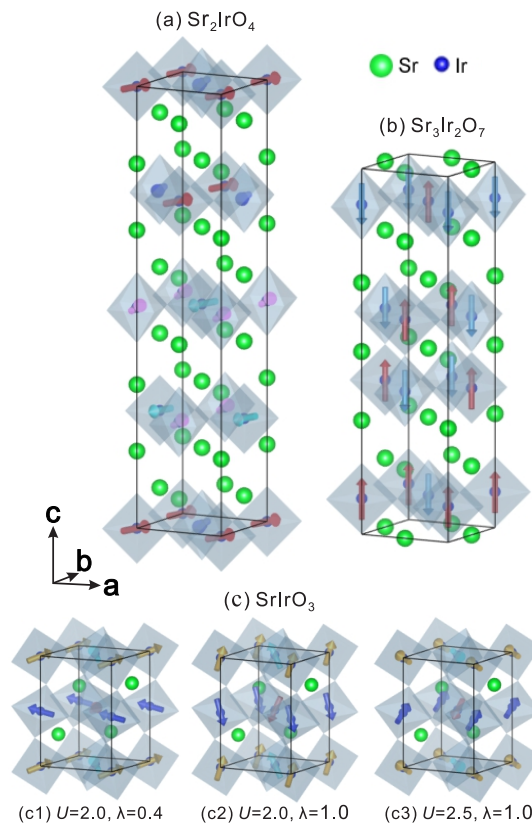
Figure 7. Magnetic orderings of three iridates predicted by the LSDA+U+SOC method: (**a**) Sr_2IrO_4 with $U = 1.82$ eV and $\lambda = 1.0$; (**b**) $Sr_3Ir_2O_7$ with $U = 1.67$ eV and $\lambda = 1.0$; and (**c**) $SrIrO_3$, for which the magnetic structure depends strongly on the values of U and λ in the magnetic regime (see Figure 2). The arrows denote the magnetic moment of each Ir atom. Sr and Ir are shown in green and blue, respectively. O atoms are not shown.

Having obtained the magnetic ground states for three iridates, we are now in a position to explain why Sr_2IrO_4 exhibits an unusual *ab*-canted AFM, whereas the structurally similar compound $Sr_3Ir_2O_7$ shows a *c*-collinear AFM. The former has been largely discussed in Reference [14]. Here, we just summarize the main points. To study the anisotropic magnetic couplings in Sr_2IrO_4, we put forward a scheme by mapping fully relativistic constrained noncollinear LSDA+U calculations onto a general spin model Hamiltonian:

$$\Delta E = -\sum_{i<j} \mathbf{J}_{ij}\mathbf{S}_i \cdot \mathbf{S}_j + \sum_i \varepsilon_{an}^i(\mathbf{S}_i) + \sum_{i<j} \mathbf{D}_{ij} \cdot [\mathbf{S}_i \times \mathbf{S}_j], \tag{24}$$

where the first, second, and last terms represent the isotropic AFM exchange, the single-site anisotropy (SSA), and Dzyaloshinskii–Moriya interactions, respectively. After taking the sum over all the Ir ions in the conventional unit cell, Equation (24) reduces to

$$\Delta E = 16JS^2\cos(2\theta_s) + 8K\cos(4\theta_s) - 16D_zS^2\sin(2\theta_s) \tag{25}$$

where J, K, and D_z are the nearest-neighbor isotropic exchange, SSA, and DM coupling parameters, respectively, and S and θ_s are the magnitude and canted angle of the in-plane spin moment, respectively. Figure 8 shows the spin-dependent total energy as a function of the in-plane spin canting angle θ_s decomposed over the isotropic AFM exchange, SSA, and DM contributions. The magnetic coupling parameters can be extracted by fitting the first-principles calculated data using the model Equation (25), yielding $JS^2 = -0.32$ meV, $K = -0.1$ meV, and $D_zS^2 = 0.25$ meV, comparable with available phenomenological data in literature [21,159]. The AFM isotropic exchange, favoring a collinear alignment of the

spins, aids the stabilization of the AFM ordering. The DM interaction, which prefers an orthogonal coupling of the spins, assists the formation of a canted spin arrangement. The SSA is smaller than isotropic and DM interactions but favors in-plane magnetism at small canting angles. As expected, the evolution of the DM and isotropic exchange energies follows a different trend with respect to θ_s. The formation of the in-plane canted AFM state at $\theta_s = 14.4°$ is the result of the subtle competition between these three terms: JS^2, D_zS^2, and K.
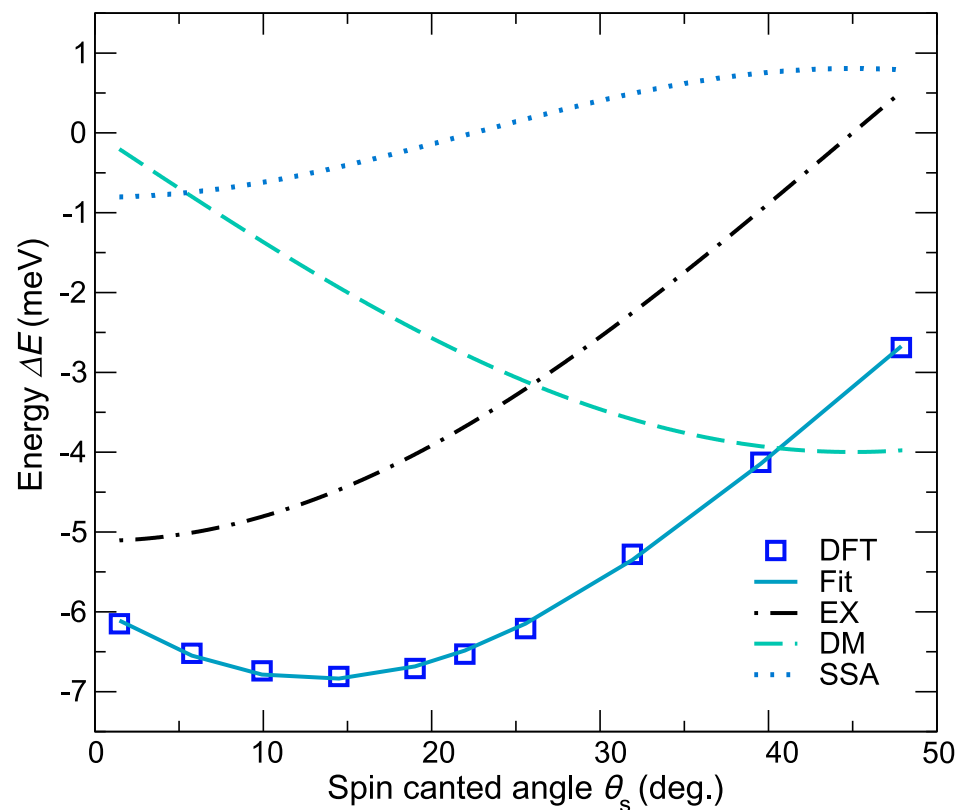

Figure 8. The spin-dependent total energy as a function of the in-plane spin canting angle θ_s decomposed over the isotropic AFM exchange (EX), SSA, and DM contributions. The zero is set such that the DM energy becomes zero for $\theta_s = 0°$. Reproduced with permission from Reference [14]. Copyright 2015 by the American Physical Society.

The *ab*-canted AFM state in Sr_2IrO_4 represents a stable magnetic ground state, but it has been found that it is susceptible to external perturbation such as small changes in the octahedral rotation angle [160], tetragonal distortions [10,14], and doping [142]. Two different types of magnetic phase transition have been predicted: *ab*-canted to *ab*-collinear by reducing the octahedral rotation angle and a transition to a *c*-collinear ordering by increasing the octahedral tetragonal distortion ($c/a \approx 1.1$). The former has been confirmed by high-pressure experimental findings [14,160].

Next, we turn to the *c*-collinear AFM magnetism of $Sr_3Ir_2O_7$. Based on the microscopic model Hamiltonian approach, Kim [33] showed that the spin–flop transition in $Sr_3Ir_2O_7$ is due to strong competition among intra- and interlayer bond-directional pseudodipolar interactions of the spin-orbit-entangled $J_{eff} = 1/2$ moments. Hence, a natural interesting question is how the magnetic ordering changes with respect to the interlayer distance, which directly controls the competition and balance between intra- and interlayer magentic couplings. Therefore, we performed an theoretical experiment by artificially increasing the interlayer distance while keeping the other local structures fixed, followed by noncollinear self-consistent total energy calculations adopting two different spin configurations: *ab*-canted AFM and *c*-collinear AFM. Figure 9 shows the total energy difference between the

ab-canted AFM and *c*-collinear AFM phases as a function of the interlayer distance. In the ground state of $Sr_3Ir_2O_7$, the interlayer distance is about 4.088 Å, where the *c*-collinear AFM phase is significantly favored compared to the *ab*-canted AFM phase. However, as the interlayer distance increases to 4.38 Å, the *ab*-canted AFM phase becomes the most energetically stable phase due to the reduced the interlayer magnetic coupling (see Figure 9). Our theoretical experiment thus suggests the important role played by interlayer coupling in the formation of the *c*-collinear AFM state of $Sr_3Ir_2O_7$.
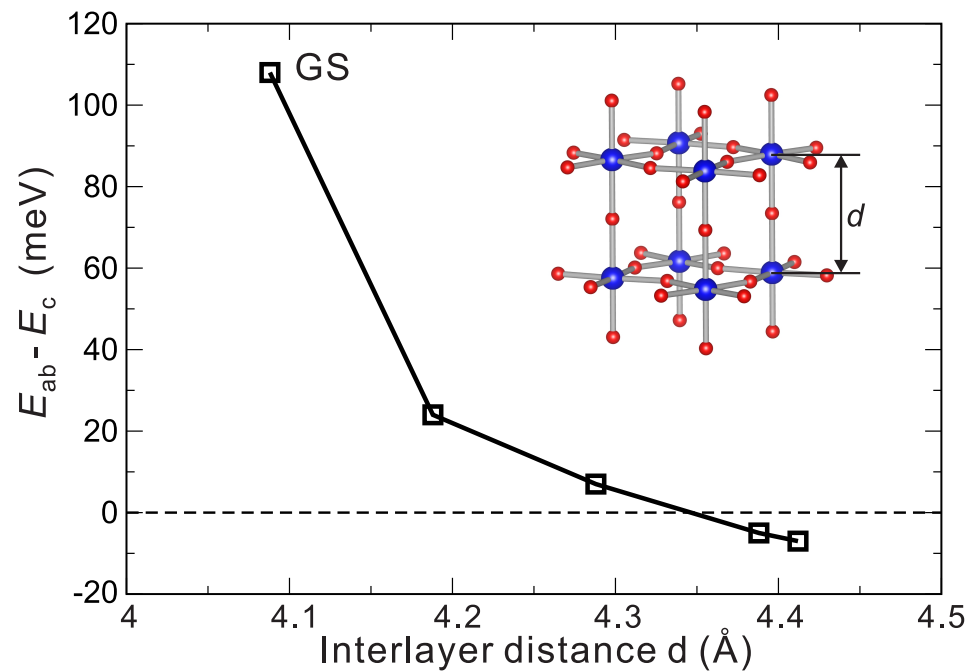

Figure 9. The total energy difference between the *ab*-canted AFM and *c*-collinear AFM phases as a function of the interlayer distance, which is schematically shown in the inset. The ground-state structure is marked as GS.

4.4. Optical Spectra

To conclude with the presentation of the fundamental properties of the RP iridates family, we briefly survey the optical characteristics in this section.

Figure 10 shows our computed optical conductivity for the considered iridates through the solution of the BSE using the QP energies and screened interactions *W* derived from the *GW* calculations. For comparison, DMFT-calculated results [154] and experimental data [18,31,36] are also given. We found that all the compounds are characterized by a double-peak structure (*α* and *β*), consistent with the experiments [18,31,36]. However, the agreement depends on the level of theory and is material-dependent. For instance, though both BSE and RPA are able to reproduce the two dominant peaks, a good quantitative agreement with experiments is only obtained at the BSE level for Sr_2IrO_4 and $Sr_3Ir_2O_7$, for which the calculated and measured *α* and *β* transitions are centered almost at the same excitation energies. As compared to RPA, the dramatic redshift of the *α* and *β* peaks predicted by BSE indicates strong excitonic effects, but no bound exciton is discerned in our BSE calculations. A double-peak structure was also observed in $SrIrO_3$, which is qualitatively consistent with the recent experimental findings by Fujioka [36]. However, the agreement between theory and experiment is less satisfactory compared to the *n* = 1 and *n* = 2 cases. For example, the calculated *α* and *β* peaks are centered at higher energies than the experimental ones [36] and the Drude peak is broader and more intense. We note that, for $SrIrO_3$, the DMFT calculations [154] reproduce relatively well the *β* peak but that the *α* peak is not detected.
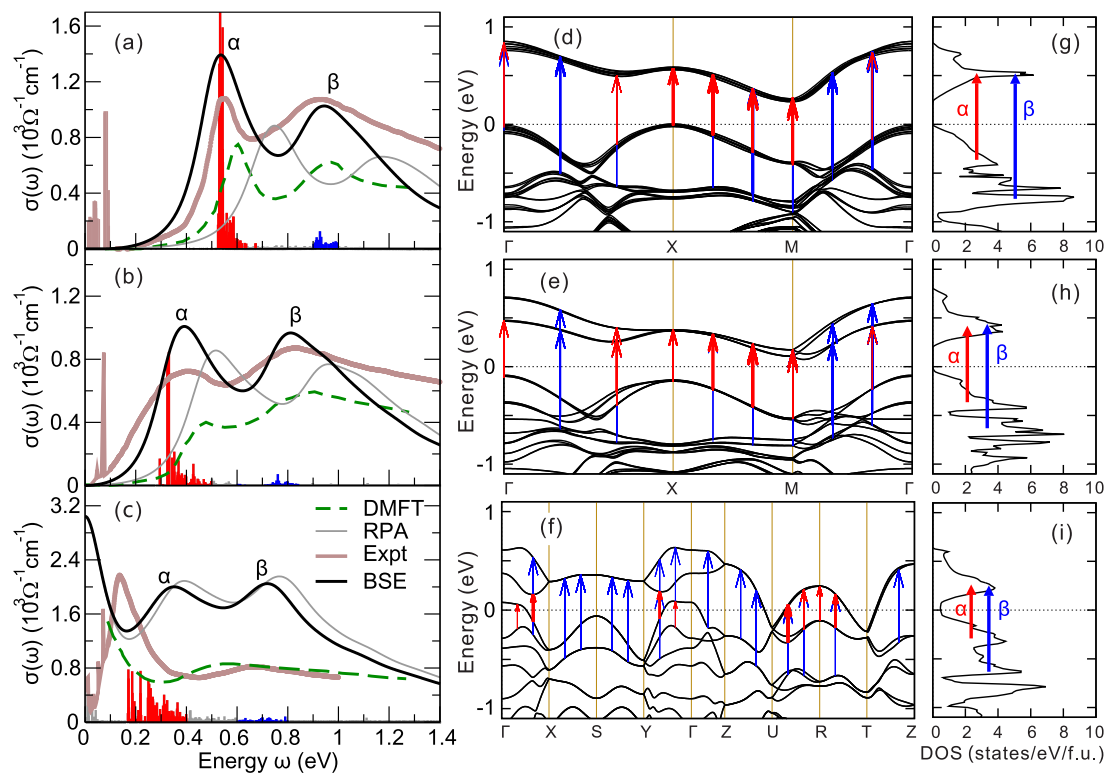
Figure 10. The experimental and calculated optical conductivity spectra $\sigma(\omega)$ of (**a**) Sr_2IrO_4, (**b**) $Sr_3Ir_2O_7$, and (**c**) $SrIrO_3$. The experimental data at 10 K are adapted from Reference [18] for Sr_2IrO_4 single crystals, Reference [31] for $Sr_3Ir_2O_7$ single crystals, and Reference [36] for $SrIrO_3$ polycrystalline samples. Note that the sharp peaks below 0.1 eV in the experimental spectra arise from optical phonon modes. The DMFT simulated spectra are taken from Reference [154]. The grey vertical lines represent the oscillator strength (divided by 10^4 here) for which the contributions to α and β peaks are highlighted in red and blue, respectively. (**d**–**f**) *GW* band structure. (**g**–**i**) *GW* total density of states. The red and blue arrows in (**d**–**f**) represent the dominant interband transitions for the α and β peaks, respectively. The width of the arrows denotes the normalized amplitude of BSE eigenvectors $|X_{cv\mathbf{k}}^{\Lambda}|$. The arrows in (**g**–**i**) show the involved optical transitions schematically. Reproduced with permission from Reference [100]. Copyright 2018 by the American Physical Society.

To identify the character of the optical transitions, the BSE oscillator strengths S_Λ (Equation (21)) were calculated and shown as histograms in Figure 10a–c. The oscillator strengths are associated with the dominant *k*-point dependent interband transitions, which are represented by arrows in the band structure plots of Figure 10d–f. We note that the width of the arrows is proportional to the corresponding amplitude of BSE eigenvectors. This analysis clearly demonstrates that the α peak arises from the optical transition from the $J_{\text{eff}} = 1/2$ LHB to the $J_{\text{eff}} = 1/2$ UHB whereas the β peak comes from $J_{\text{eff}} = 3/2$ to $J_{\text{eff}} = 1/2$ UHB excitations, as schematically evidenced in the DOS given in Figure 10g–i. Since the $J_{\text{eff}} = 1/2$ LHB and UHB are rather flat and parallel for Sr_2IrO_4, in particular along the *X–M* direction, the α-type excitations are particularly strong compared to the β-type excitations, leading to a relatively narrower width of the α peak. Moving onto $Sr_3Ir_2O_7$, the LHB and UHB split and are less parallel than those in Sr_2IrO_4. As a result, the α peak becomes less intense and broader. For $SrIrO_3$, the $J_{\text{eff}} = 1/2$ band topology is strongly perturbed due to the substantial hybridization between Ir-5*d* and O-2*p* orbitals originating from the underlying distorted three-dimensional orthorhombic crystal structure. Ultimately, this leads to admixing of the $J_{\text{eff}} = 3/2$ states with the lower $J_{\text{eff}} = 1/2$ band. As a result, the α and β peaks are much broader. However, agreement with the experiment is not satisfactory. The reasons are twofold: First, *GW* does not properly account for the strong bandwidth renormalization observed experimentally [152], which drastically changes the band topology near the Fermi level and thus affects the optical excitations. Second, it appears that there are experimental complications (difficulties in synthesizing stoichiometric

crystals, degradation in ambient conditions, sensitivity to lithographic processing, and presence of oxygen vacancies) that make it difficult to perform systematic and reproducible measurements of transport properties [161–163]. This clearly hinders a direct comparison with theory. In fact, depending on the specific type of sample (polycrystalline [36] or $SrIrO_3$ films grown on MgO [11] or $SrTiO_3$ [164]), different optical conductivity spectra have been reported in the literature which differ even in fundamental aspects such as the presence or absence of an α peak.

Finally, we found that, by going from $n = 1$ to $n = \infty$, the α and β peaks are progressively shifted towards lower energies, in agreement with experimental observations [11]. This trend is correlated with the progressive decrease in interaction U (see Table 2) and with the gradual closing of the GW gap [100].

5. Conclusions

In summary, we reviewed the fundamental properties of RP series of iridates $Sr_{n+1}Ir_nO_{3n+1}$ ($n = 1, 2$ and ∞) using an array of advanced methodological approaches: fully relativistic noncollinear LSDA+U, cRPA, GW+SOC, and BSE+SOC. Besides collecting the results that we obtained in the last five years in a thematically focused context, we also included some original results, specifically a complete U/SOC phase diagram and an analysis of the band structures disentangling the role of U and SOC. In addition, we extended the quantification of the most relevant energy scales of all three compounds.

For three compounds, the estimated crystal field energy (about 4 eV) represents the dominant energy scale, and therefore, the low-energy physics can be described by using the low-lying t_{2g} states of Ir only. The SOC strength is relatively small (≈ 0.5 eV) but comparable to the strength of the Hubbard U (≈ 1.5 eV) quantified by cRPA. The MIT transition with respect to the intermingled interactions of SOC and U provide clear evidence for the relativistic Mott–Hubbard character of the insulating state in the $n = 1$ and $n = 2$ phases. A comparative study between LSDA+U+SOC and GW+SOC shows that both methods yield similar band structures except that GW pushes down the O-2p states by about 0.5 eV and demonstrates that the predicted band gaps for Sr_2IrO_4 and $Sr_3Ir_2O_7$ are in excellent agreement with the measurements. However, both methods fail to describe the correlated semi-metallic state of $SrIrO_3$, incorrectly predicting a pseudogap at the Fermi level, and GW finds a mass enhancement of only 1.64, largely underestimated compared to experimental estimations.

Because of similar quasi-2D layered crystal structures, Sr_2IrO_4 and $Sr_3Ir_2O_7$ exhibit overall similar properties, in particular in terms of the MIT phase diagrams, electronic band structures, and optical conductivity spectra, whereas their magnetic properties are radically different. The formation of an ab-canted AFM state in Sr_2IrO_4 is a result of intermingled competition between the isotropic exchange, single-ion anisotropy, and DM interactions, and new magnetic phases (in-plane collinear AFM ordering and c-collinear AFM ordering) can be developed by tuning the balance of these magnetic interactions through octahedral distortions (octahedral rotations and tetragonal distortions). The c-collinear AFM ground state of $Sr_3Ir_2O_7$ is very robust due to strong interlayer magnetic coupling. The spin phase transition to the ab-canted AFM phase can only be achieved by increasing the interplayer distance to a very large and experimentally unobtainable value.

The computed GW+BSE optical conductivity spectra of three iridates show strong excitonic effects and reproduce the experimentally observed double-peak structure very well, in particular for Sr_2IrO_4 and $Sr_3Ir_2O_7$. However, for $SrIrO_3$, the description is less satisfactory, since GW does not account well for the correlated metallic state of $SrIrO_3$ and going beyond GW is necessary. Our analysis describes well the progressive redshift of the main optical peaks as a function of dimensionality n, which is correlated with the gradual decrease in electronic correlation U and gradual closing of the band gaps towards the metallic $n = \infty$ limit.

The major physics of the bulk phases of RP iridates are presently very well understood. Some discrepancies in the interpretation of the optical and electronic properties of the 3D

end member remain, which will hopefully be resolved in forthcoming studies. One of the most interesting conceptual and technologically relevant questions that has started to attract the scientific community is the possibility to modify and functionalize the intrinsic properties of RP iridates by means of strain engineering [165–167], which will possibly further widen the interest on iridates.

References

1. Rau, J.G.; Lee, E.K.H.; Kee, H.Y. Spin-Orbit Physics Giving Rise to Novel Phases in Correlated Systems: Iridates and Related Materials. *Annu. Rev. Condens. Matter Phys.* **2016**, *7*, 195–221. doi:10.1146/annurev-conmatphys-031115-011319.

2. Witczak-Krempa, W.; Chen, G.; Kim, Y.B.; Balents, L. Correlated Quantum Phenomena in the Strong Spin-Orbit Regime. *Annu. Rev. Condens. Matter Phys.* **2014**, *5*, 57–82. doi:10.1146/annurev-conmatphys-020911-125138.

3. Cao, G.; Schlottmann, P. The challenge of spin–orbit-tuned ground states in iridates: a key issues review. *Rep. Prog. Phys.* **2018**, *81*, 042502. doi:10.1088/1361-6633/aaa979.

4. Martins, C.; Aichhorn, M.; Biermann, S. Coulomb correlations in 4d and 5d oxides from first principles—or how spin–orbit materials choose their effective orbital degeneracies. *J. Phys. Condens. Matter* **2017**, *29*, 263001. doi:10.1088/1361-648x/aa648f.

5. Hao, L.; Meyers, D.; Dean, M.; Liu, J. Novel spin-orbit coupling driven emergent states in iridate-based heterostructures. *J. Phys. Chem. Solids* **2019**, *128*, 39 – 53. doi:10.1016/j.jpcs.2017.11.018.

6. Lu, C.; Liu, J.M. The Jeff = 1/2 Antiferromagnet Sr2IrO4: A Golden Avenue toward New Physics and Functions. *Adv. Mater.* **2020**, *32*, 1904508. doi:10.1002/adma.201904508.

7. Zhang, L.; Pang, B.; Chen, Y.B.; Chen, Y. Review of Spin-orbit Coupled Semimetal SrIrO3 in Thin Film Form. *Crit. Rev. Solid State Mater. Sci.* **2018**, *43*, 367–391. doi:10.1080/10408436.2017.1358147.

8. Kim, B.J.; Jin, H.; Moon, S.J.; Kim, J.Y.; Park, B.G.; Leem, C.S.; Yu, J.; Noh, T.; Kim, C.; Oh, S.J.; et al. Novel $J_{eff} = 1/2$ Mott State Induced by Relativistic Spin-Orbit Coupling in Sr_2IrO_4. *Phys. Rev. Lett.* **2008**, *101*, 076402. doi:10.1103/PhysRevLett.101.076402.

9. Kim, B.J.; Ohsumi, H.; Komesu, T.; Sakai, S.; Morita, T.; Takagi, H.; Arima, T. Phase-Sensitive Observation of a Spin-Orbital Mott State in Sr2IrO4. *Science* **2009**, *323*, 1329–1332. doi:10.1126/science.1167106.

10. Jackeli, G.; Khaliullin, G. Mott Insulators in the Strong Spin-Orbit Coupling Limit: From Heisenberg to a Quantum Compass and Kitaev Models. *Phys. Rev. Lett.* **2009**, *102*, 017205. doi:10.1103/PhysRevLett.102.017205.

11. Moon, S.J.; Jin, H.; Kim, K.W.; Choi, W.S.; Lee, Y.S.; Yu, J.; Cao, G.; Sumi, A.; Funakubo, H.; Bernhard, C.; et al. Dimensionality-Controlled Insulator-Metal Transition and Correlated Metallic State in 5d Transition Metal Oxides $Sr_{n+1}Ir_nO_{3n+1}$ (n = 1, 2, and ∞). *Phys. Rev. Lett.* **2008**, *101*, 226402. doi:10.1103/PhysRevLett.101.226402.

12. Yamasaki, A.; Fujiwara, H.; Tachibana, S.; Iwasaki, D.; Higashino, Y.; Yoshimi, C.; Nakagawa, K.; Nakatani, Y.; Yamagami, K.; Aratani, H.; et al. Three-dimensional electronic structures and the metal-insulator transition in Ruddlesden-Popper iridates. *Phys. Rev. B* **2016**, *94*, 115103. doi:10.1103/PhysRevB.94.115103.

13. Watanabe, H.; Shirakawa, T.; Yunoki, S. Microscopic Study of a Spin-Orbit-Induced Mott Insulator in Ir Oxides. *Phys. Rev. Lett.* **2010**, *105*, 216410. doi:10.1103/PhysRevLett.105.216410.

14. Liu, P.; Khmelevskyi, S.; Kim, B.; Marsman, M.; Li, D.; Chen, X.Q.; Sarma, D.D.; Kresse, G.; Franchini, C. Anisotropic magnetic couplings and structure-driven canted to collinear transitions in Sr_2IrO_4 by magnetically constrained noncollinear DFT. *Phys. Rev. B* **2015**, *92*, 054428. doi:10.1103/PhysRevB.92.054428.

15. Fujiyama, S.; Ohsumi, H.; Komesu, T.; Matsuno, J.; Kim, B.J.; Takata, M.; Arima, T.; Takagi, H. Two-Dimensional Heisenberg Behavior of J_{eff}=1/2 Isospins in the Paramagnetic State of the Spin-Orbital Mott Insulator Sr_2IrO_4. *Phys. Rev. Lett.* **2012**, *108*, 247212. doi:10.1103/PhysRevLett.108.247212.

16. Dhital, C.; Hogan, T.; Yamani, Z.; de la Cruz, C.; Chen, X.; Khadka, S.; Ren, Z.; Wilson, S.D. Neutron scattering study of correlated phase behavior in Sr_2IrO_4. *Phys. Rev. B* **2013**, *87*, 144405. doi:10.1103/PhysRevB.87.144405.

17. Ye, F.; Chi, S.; Chakoumakos, B.C.; Fernandez-Baca, J.A.; Qi, T.; Cao, G. Magnetic and crystal structures of Sr_2IrO_4: A neutron diffraction study. *Phys. Rev. B* **2013**, *87*, 140406. doi:10.1103/PhysRevB.87.140406.

18. Moon, S.J.; Jin, H.; Choi, W.S.; Lee, J.S.; Seo, S.S.A.; Yu, J.; Cao, G.; Noh, T.W.; Lee, Y.S. Temperature dependence of the electronic structure of the $J_{eff} = \frac{1}{2}$ Mott insulator Sr_2IrO_4 studied by optical spectroscopy. *Phys. Rev. B* **2009**, *80*, 195110. doi:10.1103/PhysRevB.80.195110.

19. Arita, R.; Kuneš, J.; Kozhevnikov, A.V.; Eguiluz, A.G.; Imada, M. Ab initio. *Phys. Rev. Lett.* **2012**, *108*, 086403. doi:10.1103/PhysRevLett.108.086403.

20. Katukuri, V.M.; Stoll, H.; van den Brink, J.; Hozoi, L. Ab initio. *Phys. Rev. B* **2012**, *85*, 220402. doi:10.1103/PhysRevB.85.220402.

21. Kim, J.; Casa, D.; Upton, M.H.; Gog, T.; Kim, Y.J.; Mitchell, J.F.; van Veenendaal, M.; Daghofer, M.; van den Brink, J.; Khaliullin, G.; et al. Magnetic Excitation Spectra of Sr_2IrO_4 Probed by Resonant Inelastic X-Ray Scattering: Establishing Links to Cuprate Superconductors. *Phys. Rev. Lett.* **2012**, *108*, 177003. doi:10.1103/PhysRevLett.108.177003.

22. Wang, F.; Senthil, T. Twisted Hubbard Model for Sr_2IrO_4: Magnetism and Possible High Temperature Superconductivity. *Phys. Rev. Lett.* **2011**, *106*, 136402. doi:10.1103/PhysRevLett.106.136402.

23. Watanabe, H.; Shirakawa, T.; Yunoki, S. Monte Carlo Study of an Unconventional Superconducting Phase in Iridium Oxide $J_{eff}{=}1/2$ Mott Insulators Induced by Carrier Doping. *Phys. Rev. Lett.* **2013**, *110*, 027002. doi:10.1103/PhysRevLett.110.027002.

24. Kim, Y.K.; Krupin, O.; Denlinger, J.D.; Bostwick, A.; Rotenberg, E.; Zhao, Q.; Mitchell, J.F.; Allen, J.W.; Kim, B.J. Fermi arcs in a doped pseudospin-1/2 Heisenberg antiferromagnet. *Science* **2014**, *345*, 187–190. doi:10.1126/science.1251151.

25. Kim, Y.K.; Sung, N.H.; Denlinger, J.D.; Kim, B.J. Observation of a d-wave gap in electron-doped Sr2IrO4. *Nat. Phys.* **2015**, *12*, 37.

26. Lupascu, A.; Clancy, J.P.; Gretarsson, H.; Nie, Z.; Nichols, J.; Terzic, J.; Cao, G.; Seo, S.S.A.; Islam, Z.; Upton, M.H.; et al. Tuning Magnetic Coupling in Sr_2IrO_4 Thin Films with Epitaxial Strain. *Phys. Rev. Lett.* **2014**, *112*, 147201. doi:10.1103/PhysRevLett.112.147201.

27. Wojek, B.M.; Berntsen, M.H.; Boseggia, S.; Boothroyd, A.T.; Prabhakaran, D.; McMorrow, D.F.; Ronnow, H.M.; Chang, J.; Tjernberg, O. The $J_{eff} = \frac{1}{2}$ insulator Sr3Ir2O7 studied by means of angle-resolved photoemission spectroscopy. *J. Phys. Condens. Matter* **2012**, *24*, 415602.

28. Wang, Q.; Cao, Y.; Waugh, J.A.; Park, S.R.; Qi, T.F.; Korneta, O.B.; Cao, G.; Dessau, D.S. Dimensionality-controlled Mott transition and correlation effects in single-layer and bilayer perovskite iridates. *Phys. Rev. B* **2013**, *87*, 245109. doi:10.1103/PhysRevB.87.245109.

29. Okada, Y.; Walkup, D.; Lin, H.; Dhital, C.; Chang, T.R.; Khadka, S.; Zhou, W.; Jeng, H.T.; Paranjape, M.; Bansil, A.; et al. Imaging the evolution of metallic states in a correlated iridate. *Nat. Mater.* **2013**, *12*, 707.

30. Fujiyama, S.; Ohashi, K.; Ohsumi, H.; Sugimoto, K.; Takayama, T.; Komesu, T.; Takata, M.; Arima, T.; Takagi, H. Weak antiferromagnetism of $J_{eff} = \frac{1}{2}$ band in bilayer iridate $Sr_3Ir_2O_7$. *Phys. Rev. B* **2012**, *86*, 174414. doi:10.1103/PhysRevB.86.174414.

31. Park, H.J.; Sohn, C.H.; Jeong, D.W.; Cao, G.; Kim, K.W.; Moon, S.J.; Jin, H.; Cho, D.Y.; Noh, T.W. Phonon-assisted optical excitation in the narrow bandgap Mott insulator $Sr_3Ir_2O_7$. *Phys. Rev. B* **2014**, *89*, 155115. doi:10.1103/PhysRevB.89.155115.

32. Boseggia, S.; Springell, R.; Walker, H.C.; Boothroyd, A.T.; Prabhakaran, D.; Collins, S.P.; McMorrow, D.F. On the magnetic structure of $Sr_3Ir_2O_7$: An X-ray resonant scattering study. *J. Phys. Condens. Matter* **2012**, *24*, 312202.

33. Kim, J.W.; Choi, Y.; Kim, J.; Mitchell, J.F.; Jackeli, G.; Daghofer, M.; van den Brink, J.; Khaliullin, G.; Kim, B.J. Dimensionality Driven Spin-Flop Transition in Layered Iridates. *Phys. Rev. Lett.* **2012**, *109*, 037204. doi:10.1103/PhysRevLett.109.037204.

34. Kim, H.S.; Chen, Y.; Kee, H.Y. Surface states of perovskite iridates AIrO3: Signatures of a topological crystalline metal with nontrivial $\mathbb{Z}_2$ index. *Phys. Rev. B* **2015**, *91*, 235103. doi:10.1103/PhysRevB.91.235103.

35. Chen, Y.; Lu, Y.M.; Kee, H.Y. Topological crystalline metal in orthorhombic perovskite iridates. *Nat. Commun.* **2015**, *6*, 6593.

36. Fujioka, J.; Okawa, T.; Yamamoto, A.; Tokura, Y. Correlated Dirac semimetallic state with unusual positive magnetoresistance in strain-free perovskite $SrIrO_3$. *Phys. Rev. B* **2017**, *95*, 121102. doi:10.1103/PhysRevB.95.121102.

37. Dudarev, S.L.; Liu, P.; Andersson, D.A.; Stanek, C.R.; Ozaki, T.; Franchini, C. Parametrization of LSDA + U for noncollinear magnetic configurations: Multipolar magnetism in UO_2. *Phys. Rev. Mater.* **2019**, *3*, 083802. doi:10.1103/PhysRevMaterials.3.083802.

38. Wahl, R. *The Crystal Lattice: Phonons, Solitons, Dislocations*; Wiley-VCH Weinheim: Berlin, Germany, 1999; p. 43.

39. Coury, M.E.A.; Dudarev, S.L.; Foulkes, W.M.C.; Horsfield, A.P.; Ma, P.W.; Spencer, J.S. Hubbard-like Hamiltonians for interacting electrons in *s*, *p*, and *d* orbitals. *Phys. Rev. B* **2016**, *93*, 075101. doi:10.1103/PhysRevB.93.075101.

40. Anisimov, V.I.; Zaanen, J.; Andersen, O.K. Band theory and Mott insulators: Hubbard U instead of Stoner I. *Phys. Rev. B* **1991**, *44*, 943–954. doi:10.1103/PhysRevB.44.943.

41. Liechtenstein, A.I.; Anisimov, V.I.; Zaanen, J. Density-functional theory and strong interactions: Orbital ordering in Mott-Hubbard insulators. *Phys. Rev. B* **1995**, *52*, R5467–R5470. doi:10.1103/PhysRevB.52.R5467.

42. Dudarev, S.L.; Botton, G.A.; Savrasov, S.Y.; Humphreys, C.J.; Sutton, A.P. Electron-energy-loss spectra and the structural stability of nickel oxide: An LSDA+U study. *Phys. Rev. B* **1998**, *57*, 1505–1509. doi:10.1103/PhysRevB.57.1505.

43. Cococcioni, M.; de Gironcoli, S. Linear response approach to the calculation of the effective interaction parameters in the LDA + U method. *Phys. Rev. B* **2005**, *71*, 035105. doi:10.1103/PhysRevB.71.035105.

44. Biermann, S.; Aryasetiawan, F.; Georges, A. First-Principles Approach to the Electronic Structure of Strongly Correlated Systems: Combining the *GW* Approximation and Dynamical Mean-Field Theory. *Phys. Rev. Lett.* **2003**, *90*, 086402. doi:10.1103/PhysRevLett.90.086402.

45. Aryasetiawan, F.; Imada, M.; Georges, A.; Kotliar, G.; Biermann, S.; Lichtenstein, A.I. Frequency-dependent local interactions and low-energy effective models from electronic structure calculations. *Phys. Rev. B* **2004**, *70*, 195104. doi:10.1103/PhysRevB.70.195104.

46. Aryasetiawan, F.; Karlsson, K.; Jepsen, O.; Schönberger, U. Calculations of Hubbard *U* from first-principles. *Phys. Rev. B* **2006**, *74*, 125106. doi:10.1103/PhysRevB.74.125106.

47. Metzner, W.; Vollhardt, D. Correlated Lattice Fermions in $d = \infty$ Dimensions. *Phys. Rev. Lett.* **1989**, *62*, 324–327. doi:10.1103/PhysRevLett.62.324.

48. Georges, A.; Kotliar, G.; Krauth, W.; Rozenberg, M.J. Dynamical mean-field theory of strongly correlated fermion systems and the limit of infinite dimensions. *Rev. Mod. Phys.* **1996**, *68*, 13–125. doi:10.1103/RevModPhys.68.13.

49. Kotliar, G.; Savrasov, S.Y.; Haule, K.; Oudovenko, V.S.; Parcollet, O.; Marianetti, C.A. Electronic structure calculations with dynamical mean-field theory. *Rev. Mod. Phys.* **2006**, *78*, 865–951. doi:10.1103/RevModPhys.78.865.

50. Held, K.; Nekrasov, I.A.; Keller, G.; Eyert, V.; Blümer, N.; McMahan, A.K.; Scalettar, R.T.; Pruschke, T.; Anisimov, V.I.; Vollhardt, D. Realistic investigations of correlated electron systems with LDA + DMFT. *Phys. Status Solidi B* **2006**, *243*, 2599–2631. doi:10.1002/pssb.200642053.

51. Held, K.; Andersen, O.K.; Feldbacher, M.; Yamasaki, A.; Yang, Y.F. Bandstructure meets many-body theory: The LDA$^+$ DMFT method. *J. Phys. Condens. Matter* **2008**, *20*, 064202. doi:10.1088/0953-8984/20/6/064202.

52. Pavarini, E.; Koch, E.; Vollhardt, D.; Lichtenstein, A.E. *The LDA+DMFT Approach to Strongly Correlated Materials: Lecture Notes of the Autumn School 2011, Hands-on LDA+DMFT; Autumn School Organized by the DFG Research Unit 1346 Dynamical Mean-Field Approach with Predictive Power for Strongly Correlated Materials at Forschungszentrum Jülich 4–7 October 2011*; Forschungszentrum, Jülich, Germany, 2011.

53. Vaugier, L.; Jiang, H.; Biermann, S. Hubbard *U* and Hund exchange *J* in transition metal oxides: Screening versus localization trends from constrained random phase approximation. *Phys. Rev. B* **2012**, *86*, 165105. doi:10.1103/PhysRevB.86.165105.

54. Marzari, N.; Vanderbilt, D. Maximally localized generalized Wannier functions for composite energy bands. *Phys. Rev. B* **1997**, *56*, 12847–12865. doi:10.1103/PhysRevB.56.12847.

55. Mostofi, A.A.; Yates, J.R.; Lee, Y.S.; Souza, I.; Vanderbilt, D.; Marzari, N. wannier90: A tool for obtaining maximally-localised Wannier functions. *Comput. Phys. Commun.* **2008**, *178*, 685–699. doi:10.1016/j.cpc.2007.11.016.

56. Van Roekeghem, A.; Ayral, T.; Tomczak, J.M.; Casula, M.; Xu, N.; Ding, H.; Ferrero, M.; Parcollet, O.; Jiang, H.; Biermann, S. Dynamical Correlations and Screened Exchange on the Experimental Bench: Spectral Properties of the Cobalt Pnictide BaCo$_2$As$_2$. *Phys. Rev. Lett.* **2014**, *113*, 266403. doi:10.1103/PhysRevLett.113.266403.

57. Tomczak, J.M.; Liu, P.; Toschi, A.; Kresse, G.; Held, K. Merging GW with DMFT and non-local correlations beyond. *Eur. Phys. J. Spec. Top.* **2017**, *226*, 2565–2590. doi:10.1140/epjst/e2017-70053-1.

58. Kutepov, A.; Haule, K.; Savrasov, S.Y.; Kotliar, G. Self-consistent *GW* determination of the interaction strength: Application to the iron arsenide superconductors. *Phys. Rev. B* **2010**, *82*, 045105. doi:10.1103/PhysRevB.82.045105.

59. Nomura, Y.; Kaltak, M.; Nakamura, K.; Taranto, C.; Sakai, S.; Toschi, A.; Arita, R.; Held, K.; Kresse, G.; Imada, M. Effective on-site interaction for dynamical mean-field theory. *Phys. Rev. B* **2012**, *86*, 085117. doi:10.1103/PhysRevB.86.085117.

60. Miyake, T.; Aryasetiawan, F. Screened Coulomb interaction in the maximally localized Wannier basis. *Phys. Rev. B* **2008**, *77*, 085122. doi:10.1103/PhysRevB.77.085122.

61. Amadon, B.; Applencourt, T.; Bruneval, F. Screened Coulomb interaction calculations: cRPA implementation and applications to dynamical screening and self-consistency in uranium dioxide and cerium. *Phys. Rev. B* **2014**, *89*, 125110. doi:10.1103/PhysRevB.89.125110.

62. Şaşıoğlu, E.; Friedrich, C.; Blügel, S. Effective Coulomb interaction in transition metals from constrained random-phase approximation. *Phys. Rev. B* **2011**, *83*, 121101. doi:10.1103/PhysRevB.83.121101.

63. Shih, B.C.; Zhang, Y.; Zhang, W.; Zhang, P. Screened Coulomb interaction of localized electrons in solids from first principles. *Phys. Rev. B* **2012**, *85*, 045132. doi:10.1103/PhysRevB.85.045132.

64. Kaltak, M. Merging GW with DMFT. Ph.D. Thesis, University of Vienna, Vienna, Austria, 2015.

65. Freysoldt, C.; Grabowski, B.; Hickel, T.; Neugebauer, J.; Kresse, G.; Janotti, A.; Van de Walle, C.G. First-principles calculations for point defects in solids. *Rev. Mod. Phys.* **2014**, *86*, 253–305. doi:10.1103/RevModPhys.86.253.

66. Hedin, L. New Method for Calculating the One-Particle Green's Function with Application to the Electron-Gas Problem. *Phys. Rev.* **1965**, *139*, A796–A823. doi:10.1103/PhysRev.139.A796.

67. Hedin, L.; Lundqvist, S. *Solid State Physics*; Academic: New York, NY, USA, 1969.

68. Rojas, H.N.; Godby, R.W.; Needs, R.J. Space-Time Method for Ab Initio Calculations of Self-Energies and Dielectric Response Functions of Solids. *Phys. Rev. Lett.* **1995**, *74*, 1827–1830. doi:10.1103/PhysRevLett.74.1827.

69. Aryasetiawan, F. *Advances in Condensed Matter Science*; Gordon and Breach: New York, NY, USA, 2000.

70. Onida, G.; Reining, L.; Rubio, A. Electronic excitations: density-functional versus many-body Green's-function approaches. *Rev. Mod. Phys.* **2002**, *74*, 601–659. doi:10.1103/RevModPhys.74.601.

71. Golze, D.; Dvorak, M.; Rinke, P. The GW Compendium: A Practical Guide to Theoretical Photoemission Spectroscopy. *Front. Chem.* **2019**, *7*, 377. doi:10.3389/fchem.2019.00377.

72. Strinati, G.; Mattausch, H.J.; Hanke, W. Dynamical Correlation Effects on the Quasiparticle Bloch States of a Covalent Crystal. *Phys. Rev. Lett.* **1980**, *45*, 290–294. doi:10.1103/PhysRevLett.45.290.

73. Strinati, G.; Mattausch, H.J.; Hanke, W. Dynamical aspects of correlation corrections in a covalent crystal. *Phys. Rev. B* **1982**, *25*, 2867–2888. doi:10.1103/PhysRevB.25.2867.

74. Hybertsen, M.S.; Louie, S.G. First-Principles Theory of Quasiparticles: Calculation of Band Gaps in Semiconductors and Insulators. *Phys. Rev. Lett.* **1985**, *55*, 1418–1421. doi:10.1103/PhysRevLett.55.1418.

75. Hybertsen, M.S.; Louie, S.G. Electron correlation in semiconductors and insulators: Band gaps and quasiparticle energies. *Phys. Rev. B* **1986**, *34*, 5390–5413. doi:10.1103/PhysRevB.34.5390.

76. Aulbur, W.G.; Jonsson, L.; Wilkins, J.W. Quasiparticle Calculations in Solids. *Solid State Phys.* **1999**, *54*, 1–218. doi:10.1016/S0081-1947(08)60248-9.

77. Van Schilfgaarde, M.; Kotani, T.; Faleev, S. Quasiparticle Self-Consistent *GW* Theory. *Phys. Rev. Lett.* **2006**, *96*, 226402. doi:10.1103/PhysRevLett.96.226402.

78. Shishkin, M.; Kresse, G. Self-consistent *GW* calculations for semiconductors and insulators. *Phys. Rev. B* **2007**, *75*, 235102. doi:10.1103/PhysRevB.75.235102.

79. Ergönenc, Z.; Kim, B.; Liu, P.; Kresse, G.; Franchini, C. Converged *GW* quasiparticle energies for transition metal oxide perovskites. *Phys. Rev. Mater.* **2018**, *2*, 024601. doi:10.1103/PhysRevMaterials.2.024601.

80. Shishkin, M.; Marsman, M.; Kresse, G. Accurate Quasiparticle Spectra from Self-Consistent GW Calculations with Vertex Corrections. *Phys. Rev. Lett.* **2007**, *99*, 246403. doi:10.1103/PhysRevLett.99.246403.

81. Holm, B.; von Barth, U. Fully self-consistent GW self-energy of the electron gas. *Phys. Rev. B* **1998**, *57*, 2108–2117. doi:10.1103/PhysRevB.57.2108.

82. Stan, A.; Dahlen, N.E.; van Leeuwen, R. Levels of self-consistency in the GW approximation. *J. Chem. Phys.* **2009**, *130*, 114105. doi:10.1063/1.3089567.

83. Kutepov, A.L. Self-consistent solution of Hedin's equations: Semiconductors and insulators. *Phys. Rev. B* **2017**, *95*, 195120. doi:10.1103/PhysRevB.95.195120.

84. Grumet, M.; Liu, P.; Kaltak, M.; Klimeš, J.; Kresse, G. Beyond the quasiparticle approximation: Fully self-consistent *GW* calculations. *Phys. Rev. B* **2018**, *98*, 155143. doi:10.1103/PhysRevB.98.155143.

85. Kutepov, A.L. Electronic structure of Na, K, Si, and LiF from self-consistent solution of Hedin's equations including vertex corrections. *Phys. Rev. B* **2016**, *94*, 155101. doi:10.1103/PhysRevB.94.155101.

86. Maggio, E.; Kresse, G. GW Vertex Corrected Calculations for Molecular Systems. *J. Chem. Theory Comput.* **2017**, *13*, 4765–4778. doi:10.1021/acs.jctc.7b00586.

87. Bruneval, F.; Gonze, X. Accurate *GW* self-energies in a plane-wave basis using only a few empty states: Towards large systems. *Phys. Rev. B* **2008**, *78*, 085125. doi:10.1103/PhysRevB.78.085125.

88. Giustino, F.; Cohen, M.L.; Louie, S.G. GW method with the self-consistent Sternheimer equation. *Phys. Rev. B* **2010**, *81*, 115105. doi:10.1103/PhysRevB.81.115105.

89. Govoni, M.; Galli, G. Large Scale GW Calculations. *J. Chem. Theory Comput.* **2015**, *11*, 2680–2696. doi:10.1021/ct500958p.

90. Umari, P.; Stenuit, G.; Baroni, S. GW quasiparticle spectra from occupied states only. *Phys. Rev. B* **2010**, *81*, 115104. doi:10.1103/PhysRevB.81.115104.

91. Foerster, D.; Koval, P.; Sánchez-Portal, D. An O(N3) implementation of Hedin's GW approximation for molecules. *J. Chem. Phys.* **2011**, *135*, 074105. doi:10.1063/1.3624731.

92. Liu, P.; Kaltak, M.; Klimeš, J.; Kresse, G. Cubic scaling *GW*: Towards fast quasiparticle calculations. *Phys. Rev. B* **2016**, *94*, 165109. doi:10.1103/PhysRevB.94.165109.

93. Wilhelm, J.; Golze, D.; Talirz, L.; Hutter, J.; Pignedoli, C.A. Toward GW Calculations on Thousands of Atoms. *J. Phys. Chem. Lett.* **2018**, *9*, 306–312. doi:10.1021/acs.jpclett.7b02740.

94. Kim, M.; Martyna, G.J.; Ismail-Beigi, S. Complex-time shredded propagator method for large-scale *GW* calculations. *Phys. Rev. B* **2020**, *101*, 035139. doi:10.1103/PhysRevB.101.035139.

95. Ben, M. D.; Yang, C.; Li, Z.; da Jornada, F. H.; Louie, S. G.; Deslippe, J. *SC '20: Proceedings of the International Conference for High Performance Computing, Networking, Storage and Analysis, Atlanta, GA, USA, 9–19 November 2020*; IEEE Press: New York, NY, USA, 2020.

96. Bruneval, F.; Marques, M.A.L. Benchmarking the Starting Points of the GW Approximation for Molecules. *J. Chem. Theory Comput.* **2013**, *9*, 324–329. doi:10.1021/ct300835h.

97. Fuchs, F.; Furthmüller, J.; Bechstedt, F.; Shishkin, M.; Kresse, G. Quasiparticle band structure based on a generalized Kohn-Sham scheme. *Phys. Rev. B* **2007**, *76*, 115109. doi:10.1103/PhysRevB.76.115109.

98. Jiang, H.; Gomez-Abal, R.I.; Rinke, P.; Scheffler, M. Localized and Itinerant States in Lanthanide Oxides United by *GW* @ LDA + *U*. *Phys. Rev. Lett.* **2009**, *102*, 126403. doi:10.1103/PhysRevLett.102.126403.

99. Jiang, H.; Gomez-Abal, R.I.; Rinke, P.; Scheffler, M. First-principles modeling of localized *d* states with the *GW*@LDA + *U* approach. *Phys. Rev. B* **2010**, *82*, 045108. doi:10.1103/PhysRevB.82.045108.

100. Liu, P.; Kim, B.; Chen, X.Q.; Sarma, D.D.; Kresse, G.; Franchini, C. Relativistic *GW*+BSE study of the optical properties of Ruddlesden-Popper iridates. *Phys. Rev. Mater.* **2018**, *2*, 075003. doi:10.1103/PhysRevMaterials.2.075003.

101. Held, K. Electronic structure calculations using dynamical mean field theory. *Adv. Phys.* **2007**, *56*, 829–926. doi:10.1080/00018730701619647.

102. Boehnke, L.; Nilsson, F.; Aryasetiawan, F.; Werner, P. When strong correlations become weak: Consistent merging of *GW* and DMFT. *Phys. Rev. B* **2016**, *94*, 201106. doi:10.1103/PhysRevB.94.201106.

103. Nilsson, F.; Boehnke, L.; Werner, P.; Aryasetiawan, F. Multitier self-consistent *GW* + EDMFT. *Phys. Rev. Mater.* **2017**, *1*, 043803. doi:10.1103/PhysRevMaterials.1.043803.

104. Ren, X.; Rinke, P.; Joas, C.; Scheffler, M. Random-phase approximation and its applications in computational chemistry and materials science. *J. Mater. Sci.* **2012**, *47*, 7447–7471.

105. Chen, G.P.; Voora, V.K.; Agee, M.M.; Balasubramani, S.G.; Furche, F. Random-Phase Approximation Methods. *Annu. Rev. Phys. Chem.* **2017**, *68*, 421–445. doi:10.1146/annurev-physchem-040215-112308.

106. Hanke, W.; Sham, L.J. Many-particle effects in the optical spectrum of a semiconductor. *Phys. Rev. B* **1980**, *21*, 4656–4673. doi:10.1103/PhysRevB.21.4656.

107. Rohlfing, M.; Louie, S.G. Excitonic Effects and the Optical Absorption Spectrum of Hydrogenated Si Clusters. *Phys. Rev. Lett.* **1998**, *80*, 3320–3323. doi:10.1103/PhysRevLett.80.3320.

108. Benedict, L.X.; Shirley, E.L.; Bohn, R.B. Optical Absorption of Insulators and the Electron-Hole Interaction: An Ab Initio Calculation. *Phys. Rev. Lett.* **1998**, *80*, 4514–4517. doi:10.1103/PhysRevLett.80.4514.

109. Strinati, G. Effects of dynamical screening on resonances at inner-shell thresholds in semiconductors. *Phys. Rev. B* **1984**, *29*, 5718–5726. doi:10.1103/PhysRevB.29.5718.

110. Rohlfing, M.; Louie, S.G. Electron-Hole Excitations in Semiconductors and Insulators. *Phys. Rev. Lett.* **1998**, *81*, 2312–2315. doi:10.1103/PhysRevLett.81.2312.

111. Albrecht, S.; Reining, L.; Del Sole, R.; Onida, G. Ab Initio Calculation of Excitonic Effects in the Optical Spectra of Semiconductors. *Phys. Rev. Lett.* **1998**, *80*, 4510–4513. doi:10.1103/PhysRevLett.80.4510.

112. Bussi, G. Effects of the Electron-Hole Interaction on the Optical Properties of Materials: the Bethe-Salpeter Equation. *Phys. Scr.* **2004**, *T109*, 141. doi:10.1238/physica.topical.109a00141.

113. Blase, X.; Duchemin, I.; Jacquemin, D. The Bethe-Salpeter equation in chemistry: relations with TD-DFT, applications and challenges. *Chem. Soc. Rev.* **2018**, *47*, 1022–1043. doi:10.1039/C7CS00049A.

114. Sharifzadeh, S. Many-body perturbation theory for understanding optical excitations in organic molecules and solids. *J. Phys. Condens. Matter* **2018**, *30*, 153002. doi:10.1088/1361-648x/aab0d1.

115. Rohlfing, M.; Louie, S.G. Electron-hole excitations and optical spectra from first principles. *Phys. Rev. B* **2000**, *62*, 4927–4944. doi:10.1103/PhysRevB.62.4927.

116. Tiago, M.L.; Chelikowsky, J.R. Optical excitations in organic molecules, clusters, and defects studied by first-principles Green's function methods. *Phys. Rev. B* **2006**, *73*, 205334. doi:10.1103/PhysRevB.73.205334.

117. Körbel, S.; Boulanger, P.; Duchemin, I.; Blase, X.; Marques, M.A.L.; Botti, S. Benchmark Many-Body GW and Bethe-Salpeter Calculations for Small Transition Metal Molecules. *J. Chem. Theory Comput.* **2014**, *10*, 3934–3943. doi:10.1021/ct5003658.

118. He, J.; Hummer, K.; Franchini, C. Stacking effects on the electronic and optical properties of bilayer transition metal dichalcogenides MoS_2, $MoSe_2$, WS_2, and WSe_2. *Phys. Rev. B* **2014**, *89*, 075409. doi:10.1103/PhysRevB.89.075409.

119. Cunningham, B.; Grüning, M.; Azarhoosh, P.; Pashov, D.; van Schilfgaarde, M. Effect of ladder diagrams on optical absorption spectra in a quasiparticle self-consistent *GW* framework. *Phys. Rev. Mater.* **2018**, *2*, 034603. doi:10.1103/PhysRevMaterials.2.034603.

120. Franchini, C.; Sanna, A.; Marsman, M.; Kresse, G. Structural, vibrational, and quasiparticle properties of the Peierls semiconductor $BaBiO_3$: A hybrid functional and self-consistent GW + vertex-corrections study. *Phys. Rev. B* **2010**, *81*, 085213. doi:10.1103/PhysRevB.81.085213.

121. Sponza, L.; Véniard, V.; Sottile, F.; Giorgetti, C.; Reining, L. Role of localized electrons in electron-hole interaction: The case of $SrTiO_3$. *Phys. Rev. B* **2013**, *87*, 235102. doi:10.1103/PhysRevB.87.235102.

122. Gatti, M.; Sottile, F.; Reining, L. Electron-hole interactions in correlated electron materials: Optical properties of vanadium dioxide from first principles. *Phys. Rev. B* **2015**, *91*, 195137. doi:10.1103/PhysRevB.91.195137.

123. Sander, T.; Maggio, E.; Kresse, G. Beyond the Tamm-Dancoff approximation for extended systems using exact diagonalization. *Phys. Rev. B* **2015**, *92*, 045209. doi:10.1103/PhysRevB.92.045209.

124. Gross, E.K.U.; Kohn, W. Local density-functional theory of frequency-dependent linear response. *Phys. Rev. Lett.* **1985**, *55*, 2850–2852. doi:10.1103/PhysRevLett.55.2850.

125. Runge, E.; Gross, E.K.U. Density-Functional Theory for Time-Dependent Systems. *Phys. Rev. Lett.* **1984**, *52*, 997–1000. doi:10.1103/PhysRevLett.52.997.

126. Botti, S.; Schindlmayr, A.; Sole, R.D.; Reining, L. Time-dependent density-functional theory for extended systems. *Rep. Prog. Phys.* **2007**, *70*, 357–407. doi:10.1088/0034-4885/70/3/r02.

127. Marini, A.; Del Sole, R.; Rubio, A. Bound Excitons in Time-Dependent Density-Functional Theory: Optical and Energy-Loss Spectra. *Phys. Rev. Lett.* **2003**, *91*, 256402. doi:10.1103/PhysRevLett.91.256402.

128. Reining, L.; Olevano, V.; Rubio, A.; Onida, G. Excitonic Effects in Solids Described by Time-Dependent Density-Functional Theory. *Phys. Rev. Lett.* **2002**, *88*, 066404. doi:10.1103/PhysRevLett.88.066404.

129. Sottile, F.; Olevano, V.; Reining, L. Parameter-Free Calculation of Response Functions in Time-Dependent Density-Functional Theory. *Phys. Rev. Lett.* **2003**, *91*, 056402. doi:10.1103/PhysRevLett.91.056402.

130. Adragna, G.; Del Sole, R.; Marini, A. Ab initio calculation of the exchange-correlation kernel in extended systems. *Phys. Rev. B* **2003**, *68*, 165108. doi:10.1103/PhysRevB.68.165108.

131. Sharma, S.; Dewhurst, J.K.; Sanna, A.; Gross, E.K.U. Bootstrap Approximation for the Exchange-Correlation Kernel of Time-Dependent Density-Functional Theory. *Phys. Rev. Lett.* **2011**, *107*, 186401. doi:10.1103/PhysRevLett.107.186401.

132. Rigamonti, S.; Botti, S.; Veniard, V.; Draxl, C.; Reining, L.; Sottile, F. Estimating Excitonic Effects in the Absorption Spectra of Solids: Problems and Insight from a Guided Iteration Scheme. *Phys. Rev. Lett.* **2015**, *114*, 146402. doi:10.1103/PhysRevLett.114.146402.

133. Yang, Z.H.; Sottile, F.; Ullrich, C.A. Simple screened exact-exchange approach for excitonic properties in solids. *Phys. Rev. B* **2015**, *92*, 035202. doi:10.1103/PhysRevB.92.035202.

134. Refaely-Abramson, S.; Jain, M.; Sharifzadeh, S.; Neaton, J.B.; Kronik, L. Solid-state optical absorption from optimally tuned time-dependent range-separated hybrid density functional theory. *Phys. Rev. B* **2015**, *92*, 081204. doi:10.1103/PhysRevB.92.081204.

135. Wing, D.; Haber, J.B.; Noff, R.; Barker, B.; Egger, D.A.; Ramasubramaniam, A.; Louie, S.G.; Neaton, J.B.; Kronik, L. Comparing time-dependent density functional theory with many-body perturbation theory for semiconductors: Screened range-separated hybrids and the *GW* plus Bethe-Salpeter approach. *Phys. Rev. Mater.* **2019**, *3*, 064603. doi:10.1103/PhysRevMaterials.3.064603.

136. Sun, J.; Yang, J.; Ullrich, C.A. Low-cost alternatives to the Bethe-Salpeter equation: Towards simple hybrid functionals for excitonic effects in solids. *Phys. Rev. Res.* **2020**, *2*, 013091. doi:10.1103/PhysRevResearch.2.013091.

137. Bokdam, M.; Sander, T.; Stroppa, A.; Picozzi, S.; Sarma, D.D.; Franchini, C.; Kresse, G. Role of Polar Phonons in the Photo Excited State of Metal Halide Perovskites. *Sci. Rep.* **2016**, *6*, 28618.

138. Tal, A.; Liu, P.; Kresse, G.; Pasquarello, A. Accurate optical spectra through time-dependent density functional theory based on screening-dependent hybrid functionals. *Phys. Rev. Res.* **2020**, *2*, 032019. doi:10.1103/PhysRevResearch.2.032019.

139. Kresse, G.; Hafner, J. Ab initio. *Phys. Rev. B* **1993**, *47*, 558–561. doi:10.1103/PhysRevB.47.558.

140. Kresse, G.; Furthmüller, J. Efficient iterative schemes for ab initio total-energy calculations using a plane-wave basis set. *Phys. Rev. B* **1996**, *54*, 11169–11186. doi:10.1103/PhysRevB.54.11169.

141. Perdew, J.P.; Burke, K.; Ernzerhof, M. Generalized Gradient Approximation Made Simple. *Phys. Rev. Lett.* **1996**, *77*, 3865–3868. doi:10.1103/PhysRevLett.77.3865.

142. Liu, P.; Reticcioli, M.; Kim, B.; Continenza, A.; Kresse, G.; Sarma, D.D.; Chen, X.Q.; Franchini, C. Electron and hole doping in the relativistic Mott insulator $\mathbf{Sr_2IrO_4}$: A first-principles study using band unfolding technique. *Phys. Rev. B* **2016**, *94*, 195145. doi:10.1103/PhysRevB.94.195145.

143. Beznosikov, B.V.; Aleksandrov, K.S. Perovskite-like crystals of the Ruddlesden-Popper series. *Crystallogr. Rep.* **2000**, *45*, 792–798.

144. Crawford, M.K.; Subramanian, M.A.; Harlow, R.L.; Fernandez-Baca, J.A.; Wang, Z.R.; Johnston, D.C. Structural and magnetic studies of Sr_2IrO_4. *Phys. Rev. B* **1994**, *49*, 9198–9201. doi:10.1103/PhysRevB.49.9198.

145. Subramanian, M.; Crawford, M.; Harlow, R. Single crystal structure determination of double layered strontium iridium oxide [Sr3Ir2O7]. *Mater. Res. Bull.* **1994**, *29*, 645–650. doi:10.1016/0025-5408(94)90120-1.

146. Longo, J.; Kafalas, J.; Arnott, R. Structure and properties of the high and low pressure forms of SrIrO3. *J. Solid State Chem.* **1971**, *3*, 174–179. doi:10.1016/0022-4596(71)90022-3.

147. Zhao, J.G.; Yang, L.X.; Yu, Y.; Li, F.Y.; Yu, R.C.; Fang, Z.; Chen, L.C.; Jin, C.Q. High-pressure synthesis of orthorhombic SrIrO3 perovskite and its positive magnetoresistance. *J. Appl. Phys.* **2008**, *103*, 103706. doi:10.1063/1.2908879.

148. Zeb, M.A.; Kee, H.Y. Interplay between spin-orbit coupling and Hubbard interaction in SrIrO$_3$ and related *Pbnm* perovskite oxides. *Phys. Rev. B* **2012**, *86*, 085149. doi:10.1103/PhysRevB.86.085149.

149. Andlauer, B.; Schneider, J.; Tolksdorf, W. Optical Absorption, Fluorescence, and Electron Spin Resonance of Ir4+ on Octahedral Sites in Y3Ga5O12. *Phys. Status Solidi B* **1976**, *73*, 533–540. doi:10.1002/pssb.2220730220.

150. Carter, J.M.; Shankar, V.V.; Zeb, M.A.; Kee, H.Y. Semimetal and Topological Insulator in Perovskite Iridates. *Phys. Rev. B* **2012**, *85*, 115105. doi:10.1103/PhysRevB.85.115105.

151. Liu, Y.; Masumoto, H.; Goto, T. Structural, Electrical and Optical Characterization of SrIrO3 Thin Films Prepared by Laser-Ablation. *Mater. Trans.* **2005**, *46*, 100.

152. Nie, Y.F.; King, P.D.C.; Kim, C.H.; Uchida, M.; Wei, H.I.; Faeth, B.D.; Ruf, J.P.; Ruff, J.P.C.; Xie, L.; Pan, X.; et al. Interplay of Spin-Orbit Interactions, Dimensionality, and Octahedral Rotations in Semimetallic SrIrO$_3$. *Phys. Rev. Lett.* **2015**, *114*, 016401. doi:10.1103/PhysRevLett.114.016401.

153. De la Torre, A.; McKeown Walker, S.; Bruno, F.Y.; Riccó, S.; Wang, Z.; Gutierrez Lezama, I.; Scheerer, G.; Giriat, G.; Jaccard, D.; Berthod, C.; et al. Collapse of the Mott Gap and Emergence of a Nodal Liquid in Lightly Doped Sr_2IrO_4. *Phys. Rev. Lett.* **2015**, *115*, 176402. doi:10.1103/PhysRevLett.115.176402.

154. Zhang, H.; Haule, K.; Vanderbilt, D. Effective $J=1/2$ Insulating State in Ruddlesden-Popper Iridates: An LDA+DMFT Study. *Phys. Rev. Lett.* **2013**, *111*, 246402. doi:10.1103/PhysRevLett.111.246402.

155. Cao, Y.; Wang, Q.; Waugh, J.A.; Reber, T.J.; Li, H.; Zhou, X.; Parham, S.; Plumb, N.C.; Rotenberg, E.; Bostwick, A.; et al. Hallmarks of the Mott-metal crossover in the hole-doped pseudospin-1/2 Mott insulator Sr2IrO4. *Nat. Commun.* **2016**, *7*, 11367. doi:10.1038/ncomms11367.

156. Brouet, V.; Mansart, J.; Perfetti, L.; Piovera, C.; Vobornik, I.; Le Fèvre, P.; Bertran, F.M.C.; Riggs, S.C.; Shapiro, M.C.; Giraldo-Gallo, P.; et al. Transfer of spectral weight across the gap of Sr_2IrO_4 induced by La doping. *Phys. Rev. B* **2015**, *92*, 081117. doi:10.1103/PhysRevB.92.081117.

157. Cao, G.; Bolivar, J.; McCall, S.; Crow, J.E.; Guertin, R.P. Weak ferromagnetism, metal-to-nonmetal transition, and negative differential resistivity in single-crystal Sr_2IrO_4. *Phys. Rev. B* **1998**, *57*, R11039–R11042. doi:10.1103/PhysRevB.57.R11039.

158. Boseggia, S.; Walker, H.C.; Vale, J.; Springell, R.; Feng, Z.; Perry, R.S.; Sala, M.M.; Ronnow, H.M.; Collins, S.P.; McMorrow, D.F. Locking of iridium magnetic moments to the correlated rotation of oxygen octahedra in Sr_2IrO_4 revealed by x-ray resonant scattering. *J. Phys. Condens. Matter* **2013**, *25*, 422202.

159. Kim, B.H.; Khaliullin, G.; Min, B.I. Magnetic Couplings, Optical Spectra, and Spin-Orbit Exciton in 5*d* Electron Mott Insulator Sr_2IrO_4. *Phys. Rev. Lett.* **2012**, *109*, 167205. doi:10.1103/PhysRevLett.109.167205.

160. Haskel, D.; Fabbris, G.; Zhernenkov, M.; Kong, P.P.; Jin, C.Q.; Cao, G.; van Veenendaal, M. Pressure Tuning of the Spin-Orbit Coupled Ground State in Sr_2IrO_4. *Phys. Rev. Lett.* **2012**, *109*, 027204. doi:10.1103/PhysRevLett.109.027204.

161. Groenendijk, D.J.; Manca, N.; Mattoni, G.; Kootstra, L.; Gariglio, S.; Huang, Y.; van Heumen, E.; Caviglia, A.D. Epitaxial growth and thermodynamic stability of SrIrO3/SrTiO3 heterostructures. *Appl. Phys. Lett.* **2016**, *109*, 041906. doi:10.1063/1.4960101.

162. Nishio, K.; Hwang, H.Y.; Hikita, Y. Thermodynamic guiding principles in selective synthesis of strontium iridate Ruddlesden-Popper epitaxial films. *APL Mater.* **2016**, *4*, 036102. doi:10.1063/1.4943519.

163. Sung, N.H.; Gretarsson, H.; Proepper, D.; Porras, J.; Tacon, M.L.; Boris, A.V.; Keimer, B.; Kim, B.J. Crystal growth and intrinsic magnetic behaviour of Sr2IrO4. *Philos. Mag. (Abingdon)* **2016**, *96*, 413–426. doi:10.1080/14786435.2015.1134835.

164. Kim, S.Y.; Kim, C.H.; Sandilands, L.J.; Sohn, C.H.; Matsuno, J.; Takagi, H.; Kim, K.W.; Lee, Y.S.; Moon, S.J.; Noh, T.W. Manipulation of electronic structure via alteration of local orbital environment in $[(SrIrO_3)_m, (SrTiO_3)](m = 1, 2, \text{and } \infty)$ superlattices. *Phys. Rev. B* **2016**, *94*, 245113. doi:10.1103/PhysRevB.94.245113.

165. Paris, E.; Tseng, Y.; Pärschke, E.M.; Zhang, W.; Upton, M.H.; Efimenko, A.; Rolfs, K.; McNally, D.E.; Maurel, L.; Naamneh, M.; et al. Strain engineering of the charge and spin-orbital interactions in Sr2IrO4. *Proc. Natl. Acad. Sci. USA* **2020**, *117*, 24764–24770. doi:10.1073/pnas.2012043117.

166. Kim, B.; Liu, P.; Franchini, C. Magnetic properties of bilayer $Sr_3Ir_2O_7$: Role of epitaxial strain and oxygen vacancies. *Phys. Rev. B* **2017**, *95*, 024406. doi:10.1103/PhysRevB.95.024406.

167. Kim, B.; Liu, P.; Franchini, C. Dimensionality-strain phase diagram of strontium iridates. *Phys. Rev. B* **2017**, *95*, 115111. doi:10.1103/PhysRevB.95.115111.